

In Pursuit of Grid Convergence, Part I: Two-Dimensional Euler Solutions

John C. Vassberg*

Boeing Research & Technology, The Boeing Company, Huntington Beach, CA 92647

Antony Jameson†

Department of Aeronautics and Astronautics, Stanford University, Stanford, CA 94305

Abstract

Grid-convergence trends of two-dimensional Euler solutions are investigated. The airfoil geometry under study is based on the NACA0012 equation. However, unlike the NACA0012 airfoil which has a blunt-base at the trailing edge, the study geometry is extended in chord so that its trailing edge is sharp. The flow solutions utilize extremely-high-quality grids which are developed with the aid of the Karman-Trefftz conformal transformation. The topology of each grid is that of a standard O-mesh. The grids naturally extend to a farfield boundary approximately 150 chord-lengths away from the airfoil. Each quadrilateral cell of the resulting mesh has an aspect-ratio of one. The intersecting lines of the grid are essentially orthogonal at each vertex within the mesh. A family of grids is recursively derived starting with the finest mesh. Here, each successively coarser grid in the sequence is constructed by eliminating every other node of the current grid, in both computational directions. In all, a total of 8 grids comprise the family, with the coarsest-to-finest meshes having dimensions of (32×32) -to- (4096×4096) cells, respectively. Note that the finest grid in this family is comprised of over 16 million cells, and is suitable for 13 levels of multigrid. The geometry and grids are all numerically defined such that they are exactly symmetrical about the horizontal axis to ensure that a non-lifting solution is possible at zero-degrees angle-of-attack attitude. Characteristics of three well known flow solvers (FLO82, OVERFLOW & CFL3D) are studied using a matrix of four flow conditions: (subcritical and transonic) by (non-lifting and lifting). The matrix allows the ability to investigate grid-convergence trends of: 1. drag with and without lifting effects, 2. drag with and without shocks, and 3. lift and moment at constant angles-of-attack. Results presented herein use 64-bit computations and are converged to machine-level-zero residuals. All three of the flow solvers have difficulty meeting this requirement on the finest meshes, especially at the transonic flow conditions. Some unexpected results are also discussed. Take for example the subcritical cases. FLO82 solutions do not reach asymptotic grid convergence of second-order accuracy until the mesh approaches one quarter of a million cells. OVERFLOW exhibits at best a first-order accuracy for a central-difference stencil. CFL3D shows second-order accuracy for drag, but only first-order trends for lift and pitching moment. For the transonic cases, the order-of-accuracy deteriorates for all of the methods. A comparison of the limiting values of the aerodynamic coefficients is provided. Drag for the subcritical cases nearly approach zero for all of the CFD methods reviewed. These and other results are discussed.

*Boeing Technical Fellow, Fellow AIAA

†Thomas V. Jones Professor of Engineering, Fellow AIAA

Copyright © 2009 by John C. Vassberg.

Published by the American Institute of Aeronautics and Astronautics with permission.

Nomenclature

<p><i>CFD</i> Computational Fluid Dynamics</p> <p>C_d Drag Coefficient = $\frac{drag}{q_\infty C_{ref}}$</p> <p>$C_l$ Lift Coefficient = $\frac{lift}{q_\infty C_{ref}}$</p> <p>$C_m$ Pitching-Moment Coefficient</p> <p>C_P Pressure Coefficient = $\frac{P-P_\infty}{q_\infty}$</p> <p>$C_{ref}$ Airfoil Reference Chord = 1.0</p> <p><i>count</i> Drag Coefficient Unit = 0.0001</p> <p><i>DPW</i> Drag Prediction Workshop</p> <p><i>f, m, c</i> Fine, Medium, Coarse Meshes</p> <p>\mathcal{F} Functional: C_l, C_d, C_m</p> <p>\mathcal{G} Newton-Method Function</p> <p><i>h</i> Cell Size</p> <p><i>i</i> Grid Index - Circling the Airfoil</p> <p><i>j</i> Grid Index - Airfoil-to-Farfield</p> <p><i>LE</i> Airfoil Leading Edge</p> <p><i>M</i> Mach Number = $\frac{V}{a}$</p> <p><i>NC</i> Number of Cells in One Direction</p> <p><i>p</i> Order-of-Accuracy</p> <p><i>P</i> Power of Karman-Trefftz Mapping</p> <p><i>q</i> Dynamic Pressure = $\frac{1}{2}\rho V^2$</p> <p><i>r</i> Radial Coordinate</p> <p><i>R</i> Radius of a Circle</p>	<p>\mathcal{R} Ratio of Grid-Convergence Deltas</p> <p><i>RANS</i> Reynolds-Averaged Navier-Stokes</p> <p><i>t</i> Thickness of an Airfoil</p> <p><i>TE</i> Airfoil Trailing Edge</p> <p><i>V</i> Velocity</p> <p><i>x</i> Horizontal Physical Coordinate</p> <p>X_{ref} Moment Reference Center = 0.25</p> <p><i>y</i> Vertical Physical Coordinate</p> <p><i>z</i> Physical Plane: $z = x + iy$</p> <p><i>1D</i> One Dimensional</p> <p><i>2D</i> Two Dimensional</p> <p><i>3D</i> Three Dimensional</p> <p>α Angle-of-Attack</p> <p>β Normalized Error Parameter</p> <p>ξ Horizontal Mapped Coordinate</p> <p>η Vertical Mapped Coordinate</p> <p>ϵ Error of Functional</p> <p>θ Angular Coordinate</p> <p>τ TE Included Angle</p> <p>ζ Mapped Plane: $\zeta = \xi + i\eta = re^{i\theta}$</p> <p>$\rho$ Radius of Curvature</p> <p>∞ Signifies Freestream Conditions</p>
---	--

I. Introduction

In recent years, the AIAA CFD Drag Prediction Workshop (DPW) Series¹ has drawn much attention to the state-of-the-art of computational fluid dynamics (CFD) as a tool for accurate aerodynamic performance assessments of aircraft, especially in the transonic-flight regime. More specifically, the DPW Series has focused on CFD methods based on the Reynolds-averaged Navier-Stokes (RANS) equations, and on test cases concerned with predominantly-turbulent high-Reynolds-number flows. The second and third workshops (DPW-II & DPW-III) have included grid-convergence studies. These investigations have yielded mixed results. As a consequence, there may be a need for the CFD community to pause for a moment and take a fresh look at the topic of grid convergence. In order to understand the issues contributing to the grid-convergence results documented by the DPW Series for 3D RANS solutions, a systematic study of grid-convergence characteristics of each of the fundamental building blocks of a 3D RANS CFD method might be required. For example, it may be necessary to study grid-convergence properties for an algorithm on one-dimensional (1D) problems with exact solutions. For the most part, this has already been done extensively in academic settings. However, previous studies conducted on two-dimensional (2D) cases occurred at a time when the limiting factor was computational resources. In addition, 2D problems receive less investigation than 1D cases by academia, and less attention than 3D solutions by industry. This situation is the motivation for the current work presented herein which focuses on 2D Euler solutions.

This paper is organized in the following manner. Section II outlines the approach taken in this work to study grid convergence on 2D Euler flows. Section III provides a description of the subject geometry which is a slightly modified NACA0012 airfoil. Section IV gives a description of the grid-generation process and the resulting family of grids utilized for the grid-convergence studies. Section V discusses the estimation of the order-of-accuracy of a CFD method and the effects on this estimate using data with errors. Section VI provides grid-convergence trends of lift, drag and pitching-moment. Tables of data are embedded within the text, while all figures are appended to the end of the paper.

II. Approach

This section briefly outlines the approach taken in the current work to study grid-convergence properties of various CFD methods on steady-state solutions of 2D inviscid, compressible flows.

- The test case is a standard public-domain symmetric airfoil, which is defined by an analytic equation.
- All numerical calculations are performed with 64-bit computations.
- All iterative results are converged to machine-level-zero residuals.
- An extremely-high-quality O-mesh is generated about the airfoil. The discrete grid nodes of the piecewise-linear airfoil surface reside on the analytic definition.
- The O-mesh is comprised of essentially orthogonal grid lines and quadrilateral cells of aspect-ratio one. Although this class of grid is not necessarily the most efficient use of cell count, nonetheless it is adopted in this work to avoid any issues related to grid stretching or cell aspect ratios.
- All grids are constructed to be exactly symmetric about the horizontal axis. This permits the possibility of a non-lifting solution at zero degrees angle-of-attack.
- The cell dimension of the finest grid is selected as a power of 2 to help facilitate construction of a family of grids, as well as to facilitate multigrid acceleration.
- A family of eight grids is constructed (starting with the finest) by removing every other grid line in both computational directions to create the next coarser grid in the sequence. The coarsest grid utilized contains (32x32) cells, whereas the finest mesh consists of (4096x4096) elements.
- Several flow conditions are studied in order to address different attributes. A zero-lift condition at a subcritical Mach number anchors the study, while a heavily-investigated transonic flow condition frames the other extreme of this investigation. Two additional conditions are included to provide build-ups between the two extremes. The resulting 2x2 matrix of conditions is (subcritical and transonic) by (non-lifting and lifting).
- Solutions of the 2D Euler equations are obtained on all grids of the family for each freestream condition under study using FLO82. Whereas, OVERFLOW and CFL3D solutions have a focus on meshes of dimension (256x256) and larger.
- Four sets of lifting data are generated using the three CFD methods. Two sets include the influence of a point vortex on the farfield boundary condition, whereas two omit this direct effect. CFL3D is run both ways.
- The order-of-accuracy of the CFD methods is estimated using solutions from the three finest meshes of the family. These grid-convergence trends are conducted for all four flow conditions, using all three CFD methods.
- Estimates are also made for the limiting values of drag, lift and pitching-moment.
- Note that the drag of an inviscid subcritical flow is precisely zero. This is compared with the estimated limiting values of drag for the subcritical flow conditions to help quantify that the solutions on the finest meshes have indeed reached the asymptotic region of grid convergence for each of the CFD methods.

The next section describes the airfoil geometry under study.

III. NACA0012 Geometry

This section provides a description of the airfoil utilized in this study. This geometry is a slightly modified NACA0012. A detail description of this subject geometry is given below. To set the stage for working towards machine-level-zero precision, the values presented in this section are provided to 10 decimal places.

Abbott and von Doenhoff² give the analytic equation defining the NACA0012 airfoil. This defining equation and its first derivative are:

$$y(x) = \pm \frac{0.12}{0.2} (0.2969\sqrt{x} - 0.1260x - 0.3516x^2 + 0.2843x^3 - 0.1015x^4) \quad (1)$$

$$y_x(x) = \pm \frac{0.12}{0.2} \left(\frac{0.14845}{\sqrt{x}} - 0.1260 - 0.7032x + 0.8529x^2 - 0.4060x^3 \right). \quad (2)$$

The numerator of the lead terms in Eqns (1-2) (i.e., 0.12) is the "thickness" of the airfoil. The standard NACA0012 airfoil is defined over the interval: $0 \leq x \leq 1$. However, at $x = 1$, the y coordinate does not vanish, and therefore, the trailing edge is not sharp, but rather has about a 0.42%-thick blunt base.

In order to avoid issues related to the solution of inviscid flows about aft-facing steps, the airfoil chord is extended so that the trailing-edge point coincides with the neighboring root of Eqn (1). (Although the actual chord length of this airfoil is slightly greater than one, a reference chord of one is adopted throughout this work to define the nondimensional aerodynamic coefficients of lift, drag and pitching-moment.) The resulting sharp trailing-edge location is:

$$x_{TE} = 1.0089304115. \quad (3)$$

At the sharp trailing-edge location, the slope of the airfoil is:

$$y_x(x_{TE}) = \mp 0.1418768821. \quad (4)$$

Hence, the included angle of the sharp trailing-edge geometry is:

$$\tau_{TE} = 2 \operatorname{atan}(|y_x(x_{TE})|) = 0.2818725 \operatorname{rad} = 16.1501066197^\circ. \quad (5)$$

The included TE angle of Eqn (5) will be needed in the next section to transform the airfoil geometry to a near circle by means of the Karman-Trefftz mapping. Another quantity needed for this transformation is the leading-edge radius of the NACA0012. This value is given by Abbott and von Doenhoff as:

$$\rho_{LE} = 1.1019 t^2 = 1.1019 (0.12^2) = 0.01586736. \quad (6)$$

For completeness, the location and value of the maximum thickness are also provided. Here x_{tmax} is determined by finding the root of Eqn (2) in the interval: $0 \leq x \leq x_{TE}$, and $t_{max} = 2 y_{max}$.

$$x_{tmax} = 0.2998278780 \quad (7)$$

$$t_{max} = 0.1200345462$$

The next section describes the generation of the grids and the grid family used herein.

IV. Grid Generation and Family of Meshes

This section describes the grid generation adopted for this study. Recall that our approach specified that the mesh be of extremely-high quality. In order to accomplish this, the Karman-Trefftz conformal transformation³ is utilized, which is defined as:

$$\left[\frac{\zeta - \zeta_1}{\zeta - \zeta_2} \right] = \left[\frac{z - z_1}{z - z_2} \right]^P ; \quad P = \left(\frac{\pi}{2\pi - \tau} \right). \quad (8)$$

Here, $z = x + iy$ is the physical plane containing the NACA0012 contour, while $\zeta = \xi + i\eta$ is the mapped plane where the airfoil is transformed to a near circle. The singular points of the transformation are z_1, z_2 ,

and ζ_1, ζ_2 , respectively in the physical and mapped planes. τ is the trailing-edge included angle provided by Eqn (5).

Removing the corner of the trailing edge can be accomplished by placing the first singular point at the sharp trailing edge, and using the correct power of the transformation as defined in Eqn (8). Furthermore, by placing the second singular point at half the leading-edge radius inside the airfoil contour at the LE, a near circle is obtained in the mapped plane. Hence,

$$\begin{aligned} z_1 &= x_{TE} + i0 = 1.0089304115 \\ z_2 &= \frac{1}{2}\rho_{LE} + i0 = 0.0079337. \end{aligned} \tag{9}$$

Under the transformation of Eqn (8), the singular points of Eqn (9) and the leading-edge point map to the following locations.

$$\begin{aligned} \zeta_1 &= 0.77043505 \\ \zeta_2 &= 0.24642903 \\ \zeta_{LE} &= 0.20139626 \\ \zeta_{TE} &= \zeta_1. \end{aligned} \tag{10}$$

Figure 1 illustrates the Karman-Trefftz transformation, based on Eqns (1-10), of the NACA0012 airfoil contour to a near circle in the mapped plane. Note that the singular points of this transformation are depicted as symbols in this figure.

In order to generate the O-mesh about the near-circle contour in the ζ -plane, the "center" of this quasi-circle is arbitrarily set as the mid-point of the mapped chordline.

$$\zeta_c \equiv \frac{1}{2}(\zeta_{LE} + \zeta_{TE}) = 0.4859156. \tag{11}$$

Relative to this center-point, the discrete points of the quasi-circle are re-distributed by linear interpolation with constant angular spacing. Unfortunately, this interpolation in the mapped plane introduces small errors in the airfoil coordinates when transformed back to physical space. To remedy this, the z coordinates are projected back onto the airfoil contour of Eqn (1). This process is repeated until the coordinates in both the z and ζ planes of all geometry points have converged to machine-level-zero.

With the quasi-circle defined by nodes at constant- θ spacing, the field mesh is generated with concentric quasi-circles that emanate outward to the farfield boundary. To achieve quadrilateral cells with an aspect-ratio of one, the radial spacing must equal the spacing in the angular direction, hence $\Delta r = r\Delta\theta$. If the quasi-circle was actually a perfect circle of radius R_1 , the radii of the concentric circles can be defined as follows.

$$R_j = R_1 e^{\frac{(j-1)2\pi}{NC}} \quad ; \quad 1 \leq j \leq NC + 1. \tag{12}$$

Here, the j subscript signifies the grid index in the computational direction normal to the quasi-circle contour, and NC is the number of cells in the j direction. R_1 is set as the discrete arclength of the quasi-circle divided by 2π .

In order to conform the mesh to the quasi-circle at the near-field boundary, a perturbation of the perfect concentric circles of Eqn (12) is introduced:

$$r_{i,j} = \frac{r_{i,1}(R_{NC+1} - R_1) + R_{NC+1}(R_j - R_1)}{(R_{NC+1} - R_1)} \quad ; \quad 1 \leq i, j \leq NC + 1. \tag{13}$$

Here, the i subscript signifies the grid index in the angular direction that wraps around the quasi-circle. As it turns out, if $j_{max} = i_{max}$, the resulting farfield boundary is about 150 chord lengths away from the airfoil surface in the physical plane. In this work, $j_{max} = i_{max} = NC + 1$ is adopted for all grids.

To ensure that the final grid is exactly symmetric about the x-axis, the grid coordinates are processed in the following manner:

$$(\hat{x}, \hat{y})_{i,j} = \frac{1}{2} [(x, y)_{i,j} + (x, -y)_{ic,j}] \quad ; \quad 1 \leq i \leq ile, 1 \leq j \leq jmax. \tag{14}$$

where $ic = (imax + 1 - i)$ is the complementary index to i , and $ile = (\frac{NC}{2} + 1)$. Then the coordinates of the final grid are replaced with the "averaged" values of (\hat{x}, \hat{y}) ,

$$(x, y)_{i,j} = (\hat{x}, \hat{y})_{i,j}, \quad ; \quad (x, y)_{ic,j} = (\hat{x}, -\hat{y})_{i,j}, \quad ; \quad 1 \leq i \leq ile, \quad 1 \leq j \leq jmax. \quad (15)$$

Figure 2 illustrates the resulting O-mesh in the mapped plane ($NC = 128$) by application of Eqns (1-13). Applying the inverse of Eqn (1) to this mesh constructs an extremely-high quality O-mesh in the physical plane about the airfoil contour. The first five grids of the family are shown in Figures 3-8. Figure-8 provides an extreme close-up view of the last 2% of the airfoil with surrounding grid for the (512x512) mesh. In the finest mesh of our family, each cell of the (512x512) mesh is further populated with 64 cells.

The next section discusses several issues related to the estimation of the order-of-accuracy of a CFD method.

V. Estimating Order of Accuracy

Estimating the order-of-accuracy of a CFD method has been a topic of on-going discussion. For example, see Baker⁴ and Salas.⁵ Following the work of Baker in his analysis of the database generated by the 2nd Drag Prediction Workshop (DPW-II), we begin our discussion with a generalized equation of computing the order-of-accuracy.

$$(\mathcal{F}_f - \mathcal{F}_m)h_c^p + (\mathcal{F}_c - \mathcal{F}_f)h_m^p + (\mathcal{F}_m - \mathcal{F}_c)h_f^p = 0. \quad (16)$$

Here, \mathcal{F} is the discrete functional computed on fine, medium, and coarse meshes of a family of grids, signified by subscripts f, m, c , respectively. The length scale of the cells of a mesh is designated h , and the estimate of the order-of-accuracy is the power p . Eqn (16) requires $h_f < h_m < h_c$. Further, $[\mathcal{F}_c, \mathcal{F}_m, \mathcal{F}_f]$ must be a monotonic sequence.

In the present work, the family of grids has the relation

$$h_c = 2h_m = 4h_f. \quad (17)$$

Also note that

$$(\mathcal{F}_c - \mathcal{F}_f) = (\mathcal{F}_c - \mathcal{F}_m) - (\mathcal{F}_m - \mathcal{F}_f). \quad (18)$$

Combining Eqns (16-18) and manipulating gives the following relationship between the ratio of functional changes between meshes, \mathcal{R} , and an estimate for the order-of-accuracy p .

$$\mathcal{R} = \frac{(\mathcal{F}_f - \mathcal{F}_m)}{(\mathcal{F}_m - \mathcal{F}_c)} = \frac{(2^p - 1)}{(4^p - 2^p)}. \quad (19)$$

If the sequence $[\mathcal{F}_c, \mathcal{F}_m, \mathcal{F}_f]$ is monotonic, then $\mathcal{R} > 0$, and p can be solved. However, if $\mathcal{R} > 1$, the order-of-accuracy becomes negative.

In order to solve for p in Eqn (19), let

$$\mathcal{G}(p) = (4^p - 2^p)\mathcal{R} - 2^p + 1 = 0. \quad (20)$$

The first derivative of \mathcal{G} with respect to p is

$$\mathcal{G}_p(p) = \ln(4) 4^p \mathcal{R} - \ln(2) 2^p (\mathcal{R} + 1). \quad (21)$$

Now p from Eqn (19) can be solved for with the Newton method

$$p^{n+1} = p^n - \frac{\mathcal{G}(p^n)}{\mathcal{G}_p(p^n)}, \quad (22)$$

where n is the iteration count and $p^0 > p$ always yields a convergent series for $p > 0$.

In the present work, an estimate of the limiting value of \mathcal{F} as $h \rightarrow 0$ can then be computed with

$$\mathcal{F}^* = \mathcal{F}_f + \frac{(\mathcal{F}_f - \mathcal{F}_m)}{(2^p - 1)}. \quad (23)$$

Since drag for any subcritical inviscid flow is identically zero, Eqn (23) can be manipulated to estimate an alternative order-of-accuracy for drag using only the medium and fine mesh results. Here, $C_d^* = 0$, and we get

$$\bar{p} = \log_2 \left[\frac{C_{d\ m}}{C_{d\ f}} \right]. \quad (24)$$

Now, p from Eqns (16-22) can be compared to \bar{p} for trends of the subcritical cases to assess how close the CFD data have captured the asymptotic range as well as the physically-correct limiting value of drag.

Effect of Functional Error on Estimate of Order-of-Accuracy

The results of Eqns (22-23) assume that the evaluations of the functional in the monotonic sequence $[\mathcal{F}_c, \mathcal{F}_m, \mathcal{F}_f]$ are known exactly. In the state-of-the-practice, however, this is typically not the case; flow solutions are routinely not sufficiently converged to yield a valid outcome. For example, data from the Drag Prediction Workshop Series¹ has been independently reviewed by Baker⁴ and Salas⁵ with the conclusion that the DPW data are not suitable to establish an estimate on the order-of-accuracy of the CFD methods utilized in the workshops. It is for this reason that the organizers of the DPW Series plotted the aggregate of the grid-convergence data against a given metric that tends as Δx^2 . This decision was made with the understanding that the assumption of second-order accuracy may not be correct, yet is no worse than attempting to solve for p with the uncertainty of the data provided.

To better understand how an error in the discrete function evaluations can affect the estimate on the order-of-accuracy, let's assume that inaccurate values of \mathcal{F} are given. This approximate value of the discrete functional is then

$$\widehat{\mathcal{F}} = \mathcal{F} \pm \epsilon, \quad (25)$$

where

$$\epsilon = \beta |\mathcal{F}_f - \mathcal{F}_m| = \beta \mathcal{R} |\mathcal{F}_m - \mathcal{F}_c|. \quad (26)$$

Here, β is a normalized error parameter that multiplies the delta functionals between the medium and fine meshes to provide the absolute error ϵ . When an error is introduced into the functional $\widehat{\mathcal{F}}$, the evaluation of \mathcal{R} in Eqn (19) gives an erroneous result, $\widehat{\mathcal{R}}$, which can be contaminated to an extent bounded by the range

$$\left[\frac{|\mathcal{F}_f - \mathcal{F}_m| - 2\epsilon}{|\mathcal{F}_m - \mathcal{F}_c| + 2\epsilon} \right] \leq \widehat{\mathcal{R}} \leq \left[\frac{|\mathcal{F}_f - \mathcal{F}_m| + 2\epsilon}{|\mathcal{F}_m - \mathcal{F}_c| - 2\epsilon} \right]. \quad (27)$$

Combining Eqns (25-27) gives

$$\mathcal{R} \left[\frac{(1 - 2\beta)}{(1 + 2\beta\mathcal{R})} \right] \leq \widehat{\mathcal{R}} \leq \mathcal{R} \left[\frac{(1 + 2\beta)}{(1 - 2\beta\mathcal{R})} \right]. \quad (28)$$

Figure 9 illustrates the impact of errors in the functionals on the estimation of order-of-accuracy p . Here, the error bands are depicted with several values of β , specifically $[\frac{1}{16}, \frac{1}{8}, \frac{1}{4}]$. For example, if the error in the functional evaluations is characterized by $\beta = \frac{1}{8}$, then a scheme which is estimated to be first-order-accurate may actually be a scheme of order as high as 1.5, or as low as 0.3. Further, note that if $\beta \geq \frac{1}{2}$, the error in the estimate of p is unbounded from below.

To better understand the nature of the impact of functional errors on the estimate on order-of-accuracy, in the present work let's require that $\beta < \frac{1}{16}$. This requires that the absolute drag must be accurately computed to within an error of $\epsilon < 6 * 10^{-8}$ for the FLO82 subcritical cases; this is 6 counts-of-a-count in drag! In the DPW databases, which are loosely based on $h_c = 1.5h_m = 2.25h_f$, the effect of β is amplified relative to that indicated by Figure 9, however the deltas between the fine and medium meshes are much larger on the 3D RANS solutions than they are for the 2D Euler results of this study. Nonetheless, a DPW-class grid-convergence study to accurately estimate order-of-accuracy would require $\epsilon \ll 0.1$ counts.

In order to minimize the effect of an inaccurate evaluation of the discrete functionals, all flow solutions of the present work are converged to machine-level-zero steady-states using 64-bit computations. While this standard may be appropriate for the finest grid utilized in this study, eventually quadruple-precision will be required if the grids are refined much further.

Figures 10-12 provide examples of the convergence histories of residuals for FLO82, OVERFLOW, and CFL3D, respectively, for the subcritical lifting condition of $M = 0.5$, and $\alpha = 1.25^\circ$. We note that the convergence rates of the transonic conditions are considerably slower for all three methods, and therefore additional cycles are required to reach equivalently-converged solutions.

The next section discusses the results of our study on grid convergence.

VI. Results

This section provides grid-convergence trends for the three CFD methods. The CFD methods are FLO82, OVERFLOW and CFL3D; their results will be independently discussed in the subsections that follow. At the end of this section, a comparison is made of the continuum estimates of the aerodynamic coefficients for the modified NACA0012 airfoil under study.

Solutions of the 2D Euler equations for non-lifting and lifting cases at both subcritical and supersonic transonic flow conditions are investigated. The matrix of flow conditions under consideration is provided in Table I.

Table I: Matrix of Flow Conditions Studied.

(M, α)	Non-Lifting	Lifting
Subcritical	$(0.5M, 0^\circ)$	$(0.5M, 1.25^\circ)$
Transonic	$(0.8M, 0^\circ)$	$(0.8M, 1.25^\circ)$

The aerodynamic coefficients of lift, drag, and pitching-moment are based on a reference chord length of $C_{ref} = 1.0$ and a moment center of $X_{ref} = 0.25$.

Figures 13-16 provide the surface pressure distributions and flowfield Mach contours about the modified NACA0012 airfoil for the four flow conditions of Table I, as computed by FLO82 on the finest mesh of (4096×4096) cells. The Mach contours are at intervals of 0.05, and the sonic lines (if present) are highlighted in bold. Also provided are the minimum and maximum values of local Mach number in the discrete fine-mesh solution.

Figures 13-14 depict the subcritical cases of non-lifting and lifting flows, respectively. Note that the maximum local Mach number of these solutions are 0.6198906 and 0.6753743 for the non-lifting and lifting flow conditions, respectively. Recall that the drag of an inviscid subcritical flow is zero.

Similarly, Figures 15-16 depict the transonic cases of non-lifting and lifting flows. The non-lifting case exhibits a fairly strong shock on both surfaces, while the lifting condition is characterized by a very strong shock on the upper surface and a fairly weak shock on the lower surface.

Choice of this set of flow solutions allows the ability to investigate grid-convergence trends of:

1. Drag with and without lifting effects (Kutta condition),
2. Drag with and without shock effects (upwind stencil), and
3. Lift and pitching-moment at constant angle-of-attacks (farfield boundary condition).

The next subsection discusses the results of the FLO82 study. Subsections dedicated to OVERFLOW and CFL3D will then follow.

FLO82-HCUSP Grid-Convergence Study

In this subsection, the grid-convergence characteristics of the FLO82 Euler method⁶ are investigated. The upwinding utilized is the H-CUSP dissipation scheme of Jameson.⁷ In addition, FLO82 includes the influence of a point-vortex on the farfield boundary condition.

The standard mesh sequencing and multigrid solution process of FLO82 is quite convenient for the purpose of this study. During this process, the converged forces and pitching-moment at each mesh level are computed. These values, convergence histories, and plots like those of Figures 13-16 are output at each mesh level. An aggregate of the FLO82 results are tabulated in Tables IIa-IIb, for the subcritical and transonic flow conditions, respectively. Note that the $\alpha = 0^\circ$ cases do not tabulate C_l or C_m , as these quantities are all evaluated as machine-level-zero. The data in these tables also include estimates for the order-of-accuracy for each functional, as well as a Richardson extrapolation of each functional to its limiting value at the continuum where $h = 0$. For the subcritical cases, the alternative estimate of order-of-accuracy \bar{p} based on Eqn (24) is also provided.

Table IIa: FLO82-HCUSP Subcritical Data at $M = 0.5$.

Mesh		$\alpha = 0^\circ$	$\alpha = 1.25^\circ$		
NC	NC^2	C_d	C_l	C_d	C_m
32	1,024	+0.001979418	+0.181639135	+0.002482085	-0.002926241
64	4,096	+0.002270216	+0.178822451	+0.001974608	-0.002487849
128	16,384	+0.000307646	+0.180014345	+0.000298397	-0.002294411
256	65,536	-0.000013299	+0.180458183	-0.000011045	-0.002301404
512	262,144	-0.000015191	+0.180446183	-0.000015534	-0.002290609
1,024	1,048,576	-0.000005076	+0.180382615	-0.000005301	-0.002276577
2,048	4,194,304	-0.000001404	+0.180354386	-0.000001481	-0.002270586
4,096	16,777,216	-0.000000365	+0.180347832	-0.000000388	-0.002269217
Continuum		+0.000000045	+0.180345850	+0.000000050	-0.002268812
Order p		1.821	2.107	1.805	2.130
\bar{p}		1.944		1.932	

For the subcritical data of Table IIa, all aerodynamic coefficients exhibit approximately a second-order-accurate trend, with drag showing slightly less than order 2, while lift and pitching-moment indicate slightly better than order 2. Note that \bar{p} is in fairly close agreement with p where applicable. These subcritical results are very promising.

Table IIb: FLO82-HCUSP Transonic Data at $M = 0.8$.

Mesh		$\alpha = 0^\circ$	$\alpha = 1.25^\circ$		
NC	NC^2	C_d	C_l	C_d	C_m
32	1,024	+0.011451356	+0.387842746	+0.027861593	-0.042947499
64	4,096	+0.010264792	+0.372921380	+0.025487792	-0.043584427
128	16,384	+0.008500758	+0.373469550	+0.023786371	-0.043873739
256	65,536	+0.008312402	+0.368980205	+0.023357651	-0.042552941
512	262,144	+0.008328328	+0.363747900	+0.023084749	-0.041002228
1,024	1,048,576	+0.008338967	+0.360812844	+0.022934404	-0.040136414
2,048	4,194,304	+0.008341760	+0.358281928	+0.022799839	-0.039388829
4,096	16,777,216	+0.008342211	+0.357142338	+0.022737860	-0.039051466
Continuum		+0.008342298	+0.356208937	+0.022684938	-0.038774022
Order		2.631	1.151	1.118	1.148

The transonic data of Table-IIb illustrates something else altogether. Here, all aerodynamic coefficients for the lifting case exhibit a first-order-accurate character. However, the drag of the non-lifting case shows an unanticipated grid-convergence trend of order $p = 2.631$. This hyper-convergence is not well understood.

The data of Tables IIa-IIb are plotted on a log-log scale in Figures 17-24. Since these data span the full family of grids, some of the data are not in the asymptotic range. To help visually identify which of these data are clearly outside the asymptotic range, the final monotonic sequence for each case is depicted with solid symbols. Therefore, the open symbols represent data which should not be used to establish grid-convergence metrics. For FLO82, the final monotonic sequence of functionals begin with the (256x256) mesh, but entering the asymptotic range appears to require at least the (512x512) mesh consisting of 262,144 cells.

The next subsection discusses the results of the OVERFLOW study.

OVERFLOW(v2.1t) Grid-Convergence Study

In this subsection, the grid-convergence characteristics of the OVERFLOW general-purpose CFD method⁸ are investigated. The version of OVERFLOW studied is (2.1t). An initial attempt was made to conduct this study using Roe upwinding. However, the convergence of residuals stalled at values far above machine-level-zero. As a consequence, we decided to use the central-differencing scheme with all of the artificial-dissipation

parameters set to their recommended default values. The pressure boundary condition imposed at the airfoil surface is based on the momentum equation ($IBTYP = 2$) and a Riemann-invariant boundary condition was used at the farfield ($IBTYP = 47$). This farfield boundary condition does not carry the direct influence of the point vortex.

Since the previous study indicates that the coarsest three mesh levels are clearly outside the asymptotic range for FLO82, we focus our efforts here on the top five meshes of the full family. Solutions for each mesh and flow condition are started from scratch and converged to machine-level-zero. To be consistent across the family of meshes, all of the cases are run in parallel on 64 processors. The results of this study are tabulated in Tables IIIa-IIIb for the subcritical and transonic flow conditions, respectively. As before, the non-lifting cases all yield machine-level-zero coefficients of lift and pitching-moment.

Table IIIa: OVERFLOW-Central Subcritical Data at $M = 0.5$.

Mesh		$\alpha = 0^\circ$	$\alpha = 1.25^\circ$		
NC	NC^2	C_d	C_l	C_d	C_m
256	65,536	+0.000063743	+0.178960502	+0.000118671	-0.002124907
512	262,144	+0.000044712	+0.179435775	+0.000068207	-0.002191480
1,024	1,048,576	+0.000028691	+0.179627329	+0.000044071	-0.002226157
2,048	4,194,304	+0.000016232	+0.179710209	+0.000029311	-0.002243944
4,096	16,777,216	+0.000008512	+0.179747254	+0.000020951	-0.002253042
Continuum		-0.000004058	+0.179777193	+0.000010030	-0.002262569
Order		0.691	1.162	0.820	0.967
\bar{p}		0.931		0.484	

For the subcritical data of Table IIIa, all aerodynamic coefficients exhibit no better than a first-order-accurate trend. Most troubling is the non-lifting case which yields an order-of-accuracy of $p = 0.691$, and an estimate of drag at the continuum of about 4% of a count. Furthermore, \bar{p} and p do not agree well with each other where applicable.

Table IIIb: OVERFLOW-Central Transonic Data at $M = 0.8$.

Mesh		$\alpha = 0^\circ$	$\alpha = 1.25^\circ$		
NC	NC^2	C_d	C_l	C_d	C_m
256	65,536	+0.008734038	+0.353909135	+0.022964252	-0.038987812
512	262,144	+0.008493959	+0.353798330	+0.022706732	-0.038656831
1,024	1,048,576	+0.008412129	+0.353241712	+0.022593342	-0.038402691
2,048	4,194,304	+0.008376064	+0.352827907	+0.022534646	-0.038251571
4,096	16,777,216	+0.008358591	+0.352522552	+0.022500576	-0.038150471
Continuum		+0.008342171	+0.351662793	+0.022453440	-0.037946129
Order		1.046	0.438	0.785	0.580

The transonic data of Table IIIb provides some interesting results. Here, the order-of-accuracy for drag on the non-lifting case has increased to first-order, as compared with that of the subcritical non-lifting condition. In contrast, the transonic lifting cases exhibit lower order-of-accuracies than the corresponding subcritical results.

The data of Tables IIIa-IIIb are plotted on a log-log scale in Figures 25-32. All of these data monotonically vary with increasing mesh dimension. In every case, the four finest meshes of the series fall on the asymptotic slope, and even the coarsest mesh of (256x256) is close to doing the same for many of the cases.

The next subsection discusses the results of the CFL3D study.

CFL3D(v6) Grid-Convergence Study

In this subsection, the grid-convergence characteristics of the CFL3D general-purpose CFD method^{9,10} are investigated. The version of CFL3D studied is (v6). Two farfield boundary conditions ($i2d = \pm 1$) are

considered for the lifting cases of this study. One farfield boundary condition includes the effect of a point-vortex and the other does not. An initial attempt was made to conduct this study using Roe upwinding. However as with OVERFLOW, the convergence of residuals stalled at values well above machine-level-zero. As a consequence, the flux-spitting scheme of CFL3D was utilized instead. Some of the pertinent input parameters are: $ifds[i, j, k] = 0$, $rkap0[i, j, k] = \frac{1}{3}$. All solutions were run in parallel on 64 processors. Unfortunately, this setup would not provide machine-level-zero results for the (4096x4096) mesh without resorting to $CFL = -1$, which required too much elapsed time for the current work. Therefore, the data provided for CFL3D excludes this finest mesh. As it turns out, the four mesh levels of data obtained reasonably indicate that the asymptotic range of CFL3D has been captured. The results of this study are tabulated in Tables IVa-IVd for the subcritical and transonic flow conditions, respectively. As before, the non-lifting cases all yielded machine-level-zero coefficients of lift and pitching-moment.

Table IVa: CFL3D-Flux-Splitting Subcritical Data at $M = 0.5$.

Mesh		$\alpha = 0^\circ$	$\alpha = 1.25^\circ$		
NC	NC^2	C_d	C_l	C_d	C_m
256	65,536	+0.000573147	+0.178366720	+0.000649962	-0.002078508
512	262,144	+0.000131328	+0.179125033	+0.000163415	-0.002152971
1,024	1,048,576	+0.000031615	+0.179487608	+0.000048451	-0.002206480
2,048	4,194,304	+0.000007502	+0.179650543	+0.000020903	-0.002235646
Continuum		-0.000000192	+0.179783519	+0.000012221	-0.002270588
Order		2.048	1.154	2.061	0.876
\bar{p}		2.075		1.213	

Table IVb: CFL3D-Flux-Splitting+Vortex Subcritical Data at $M = 0.5$.

Mesh		$\alpha = 1.25^\circ$		
NC	NC^2	C_l	C_d	C_m
256	65,536	+0.178919799	+0.000638328	-0.002084517
512	262,144	+0.179686024	+0.000151327	-0.002159318
1,024	1,048,576	+0.180052519	+0.000036185	-0.002213043
2,048	4,194,304	+0.180217309	+0.000008575	-0.002242320
Continuum		+0.180351940	-0.000000134	-0.002277383
Order		1.153	2.060	0.876
\bar{p}			2.077	

For the subcritical data of Tables IVa-IVb, a curious trend emerges for CFL3D's order-of-accuracy assessments. Specifically, it is second-order accurate for drag, but only first-order accurate for lift and pitching-moment. This is true for the non-lifting case, the lifting case without point vortex, and the lifting case with the point-vortex influence on the farfield boundary condition. However, \bar{p} and p do not agree well with each other for the lifting case without the influence of the point vortex.

Table IVc: CFL3D-Flux-Splitting Transonic Data at $M = 0.8$.

Mesh		$\alpha = 0^\circ$	$\alpha = 1.25^\circ$		
NC	NC^2	C_d	C_l	C_d	C_m
256	65,536	+0.008894250	+0.359073197	+0.023411409	-0.040316445
512	262,144	+0.008479528	+0.357580694	+0.022902709	-0.039700797
1,024	1,048,576	+0.008376058	+0.355943711	+0.022706750	-0.039170890
2,048	4,194,304	+0.008350161	+0.354593186	+0.022606485	-0.038760613
Continuum		+0.008341516	+0.348226045	+0.022501430	-0.037353559
Order		1.998	0.278	0.967	0.369

Table IVd: CFL3D-Flux-Splitting+Vortex Transonic Data at $M = 0.8$.

Mesh		$\alpha = 1.25^\circ$		
NC	NC^2	C_l	C_d	C_m
256	65,536	+0.362292941	+0.023590480	-0.040813294
512	262,144	+0.360850141	+0.023082744	-0.040205152
1,024	1,048,576	+0.359172468	+0.022884500	-0.039664060
2,048	4,194,304	+0.357798948	+0.022782607	-0.039246655
Continuum		+0.351596613	+0.022674853	-0.037838046
Order		0.289	0.960	0.374

The transonic data of Tables IVc-IVd show that the drag for the non-lifting case retains a second-order-accurate trend, but drops to first-order for both sets of lifting data. The data for lift and pitching-moment yield very low estimates on order-of-accuracy in the $\frac{1}{4}$ to $\frac{1}{3}$ range.

The data of Tables IVa-IVd are plotted on a log-log scale in Figures 33-40. All of these data monotonically vary with increasing mesh dimension. In nearly every case, the (256x256) data falls on the trendline established by the three finer meshes of the family studied here. Even though results for the (4906x4096) mesh could not be obtained in time for this printing, it appears that the asymptotic range of CFL3D has been captured with the meshes utilized.

The next subsection compares the estimates of the continuum values as predicted by the three CFD methods under study.

Summary of Continuum Estimates

In this subsection, we compare the limiting values of the aerodynamic coefficients by extrapolating the data of the three CFD methods to the continuum. These limiting values are provided in Tables Va-Vb for the subcritical and transonic flow conditions, respectively. Also included are their minimum, maximum and spread values.

Table Va: Comparison of Continuum Estimates at $M = 0.5$.

$M = 0.5$	$\alpha = 0^\circ$	$\alpha = 1.25^\circ$		
CFD Method	C_d	C_l	C_d	C_m
FLO82	+0.000000045	+0.180345850	+0.000000050	-0.002268812
OVERFLOW v2.1t	-0.000004058	+0.179777193	+0.000010030	-0.002262569
CFL3Dv6	-0.000000192	+0.179783519	+0.000012221	-0.002270588
CFL3Dv6+Vortex	-	+0.180351940	-0.000000134	-0.002277383
Min	-0.000004058	+0.179777193	-0.000000134	-0.002277383
Max	+0.000000045	+0.180351940	+0.000012221	-0.002262569
Spread	0.000004103	0.000574747	0.000012355	0.000014814

For the subcritical cases of Table Va, the limiting values of drag from FLO82 results are very close to zero; this is true for both the non-lifting and lifting cases. The drag from CFL3D also estimates a limiting value close to zero for the non-lifting case, and for the lifting case based on the point-vortex farfield boundary condition. However, the drag from CFL3D without the point vortex is considerably larger, by almost two orders-of-magnitude. OVERFLOW predicts the largest drag for the non-lifting case of about 0.04 counts, and this increases to about 0.1 counts when lifting. The total spread between the three CFD methods on lift is about 3% and about 2% on pitching-moment; these results are somewhat discouraging for a subcritical flow.

Table Vb: Comparison of Continuum Estimates at $M = 0.8$.

$M = 0.8$	$\alpha = 0^\circ$	$\alpha = 1.25^\circ$		
CFD Method	C_d	C_l	C_d	C_m
FLO82	+0.008342298	+0.356208937	+0.022684938	-0.038774022
OVERFLOW v2.1t	+0.008342171	+0.351662793	+0.022453440	-0.037946129
CFL3Dv6	+0.008341516	+0.348226045	+0.022501430	-0.037353559
CFL3Dv6+Vortex	–	+0.351596613	+0.022674853	-0.037838046
Min	+0.008341516	+0.348226045	+0.022453440	-0.038774022
Max	+0.008342298	+0.356208937	+0.022684938	-0.037353559
Spread	0.000000782	0.007983097	0.000231508	0.001420422

In Table Vb, the case of non-lifting transonic flow has all three methods agreeing quite closely on the limiting value of drag, coming in around $C_d = 0.0083419$. For the lifting case, the spread on drag is about 1%, on lift about 2%, and about 3% for pitching-moment. Interestingly, these differences are no worse than those of the subcritical flows. Nevertheless, they are worse than we would like to see.

VII. Conclusions

Grid-convergence trends of two-dimensional Euler solutions are investigated. The airfoil geometry under study is based on the NACA0012 equation, however, is extended in chord to yield a sharp trailing edge. The flow solutions utilize extremely-high-quality grids which are developed with the aid of the Karman-Trefftz conformal transformation. The topology of each grid is that of a standard O-mesh. The grids extend to a farfield boundary approximately 150 chord-lengths away from the airfoil. Each quadrilateral cell of the resulting mesh has an aspect-ratio of one, and the intersecting grid lines are essentially orthogonal at each vertex within the mesh. A family of grids is derived from the finest mesh, whereas each successively coarser grid in the sequence is constructed by eliminating every other node, in both computational directions. In all, a total of 8 grids comprise the family, with the coarsest-to-finest meshes having dimensions of (32×32) -to- (4096×4096) cells, respectively. The finest grid in this family is comprised of over 16 million cells, and is suitable for 13 levels of multigrid. The geometry and grids are all defined such that they are exactly symmetrical about the horizontal axis to ensure that a non-lifting solution is possible at zero-degrees angle-of-attack attitude.

Issues related to estimating the order-of-accuracy of a CFD method are discussed. These include the effect of errors introduced into the discrete functionals, which may arise due to insufficiently-converged flow solutions. It is possible to determine the maximum allowable error that provides an assessment to the order-of-accuracy to a desired tolerance. Based on this error analysis, quadruple-precision will eventually be required if the grid family of the present study is extended to include finer meshes.

Characteristics of three well known flow solvers (FLO82, OVERFLOW & CFL3D) are studied using a matrix of four flow conditions: (subcritical and transonic) by (non-lifting and lifting). The matrix allows the ability to investigate grid-convergence trends of: 1. drag with and without lifting effects, 2. drag with and without shocks, and 3. lift and moment at constant angle-of-attacks. The asymptotic range of FLO82 appears to begin with the (512×512) mesh, whereas the asymptotic ranges of OVERFLOW and CFL3D seem to begin with the (256×256) mesh. Second-order-accurate trendlines are demonstrated on the subcritical flow conditions for FLO82 and CFL3D. For the transonic non-lifting condition, FLO82 and CFL3D continue to show second-order accuracy. However, for the transonic lifting case, both CFD methods drop to first-order. The order-of-accuracy for OVERFLOW at all flow conditions is at best first order.

Four sets of subcritical lifting data from the three CFD methods are provided. FLO82 with the influence of a point vortex on the farfield boundary, OVERFLOW without it, and CFL3D with and without this effect. It is interesting to note that the solution sets which include the point vortex yield limiting values of drag which are much closer to zero than do the solution sets which omit the point-vortex effect.

The asymptotic behavior of the flow solution near the singular point of the trailing edge could impact the accuracy of the numerical integrations of the forces and pitching-moment. This and other issues will be addressed in our on-going work in pursuit of grid convergence.

References

- ¹4th AIAA CFD Drag Prediction Workshop. <http://aaac.larc.nasa.gov/tsab/cfdlarc/aiaa-dpw/>, dpw@cessna.textron.com, San Antonio, TX, June 2009.
- ²I. H. Abbott and A. E. von Doenhoff. *Theory of Wing Sections*. Dover, New York, 1959. ISBN 0-486-60586-8.
- ³L. M. Milne-Thomson. *Theoretical Aerodynamics*. Dover, New York, 1958. ISBN 0-486-61980-X.
- ⁴T. J. Baker. Mesh generation: Art or science? *Progress in Aerospace Sciences*, 41:29–63, 2005.
- ⁵M. D. Salas. Digital flight: The last CFD aeronautical grand challenge. *Journal of Scientific Computing*, Vol. 28, No. 213, pages 479–505, September 2006.
- ⁶A. Jameson. Solution of the Euler equations for two dimensional transonic flow by a multigrid method. *Applied Mathematics and Computation*, 13:327–356, 1983.
- ⁷A. Jameson. Artificial diffusion, upwind biasing, limiters and their effect on accuracy and multigrid convergence in transonic and hypersonic flows. *AIAA paper 93-3359*, AIAA 11th Computational Fluid Dynamics Conference, Orlando, Florida, July 1993.
- ⁸R. H. Nichols and P. G. Buning. OVERFLOW User’s Manual, Version 2.1t. Technical report, U. of Alabama and NASA, August 2008.
- ⁹S. L. Krist, R. T. Biedron, and C. L. Rumsey. CFL3D User’s Manual. *NASA-TM 1998-208444*, NASA, June 1998. Version 5.0.
- ¹⁰CFL3D Version 6.4. <http://cfl3d.larc.nasa.gov/Cfl3dv6/cfl3dv6.html>, 2006.

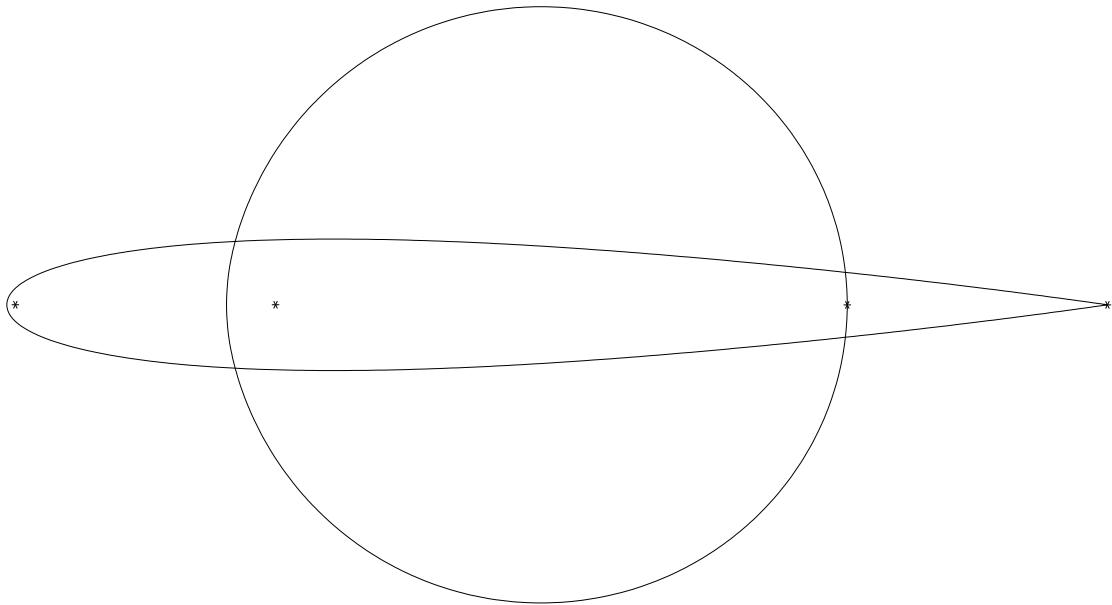


Figure 1. NACA0012 Airfoil in Physical and Transformed Planes.

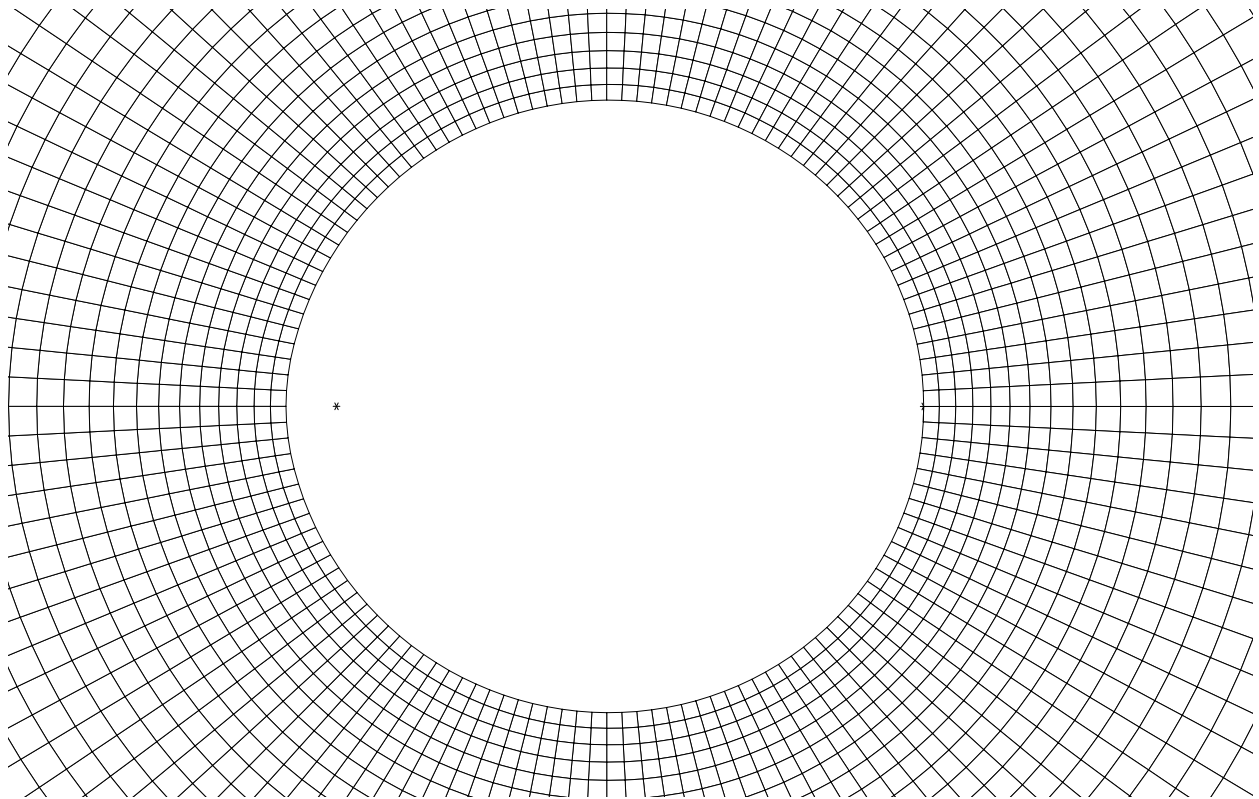


Figure 2. Close-up view of the 128x128 O-mesh in the Transformed Plane.

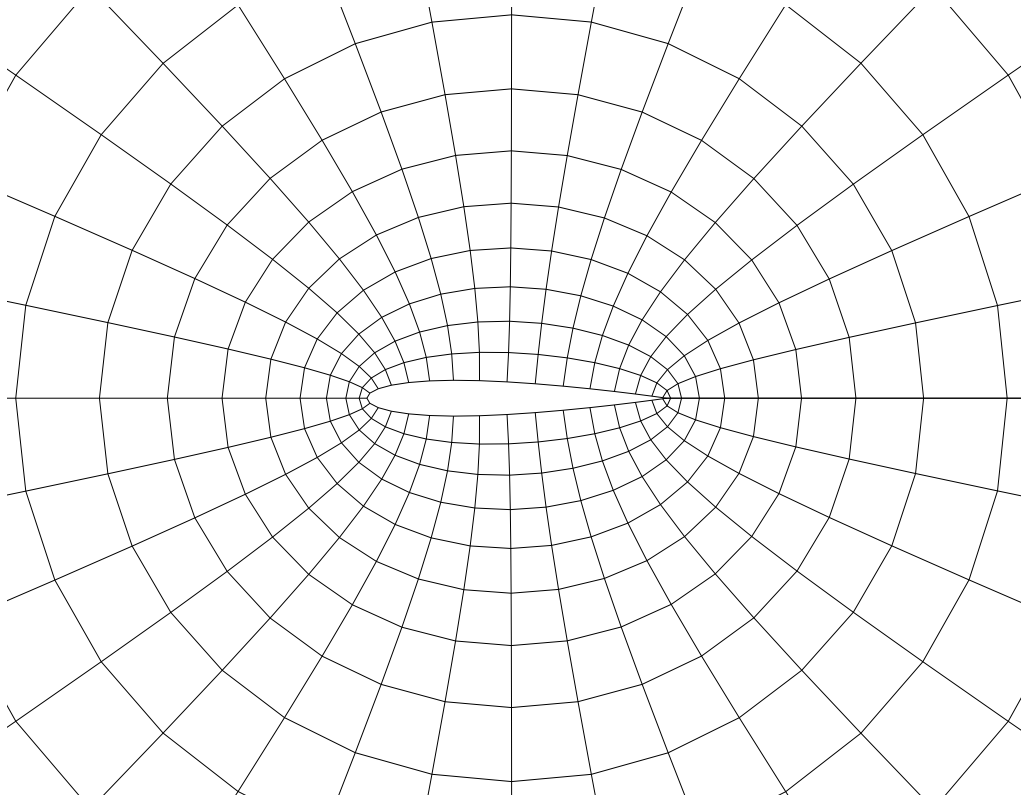


Figure 3. Close-up view of the 32x32 O-mesh.

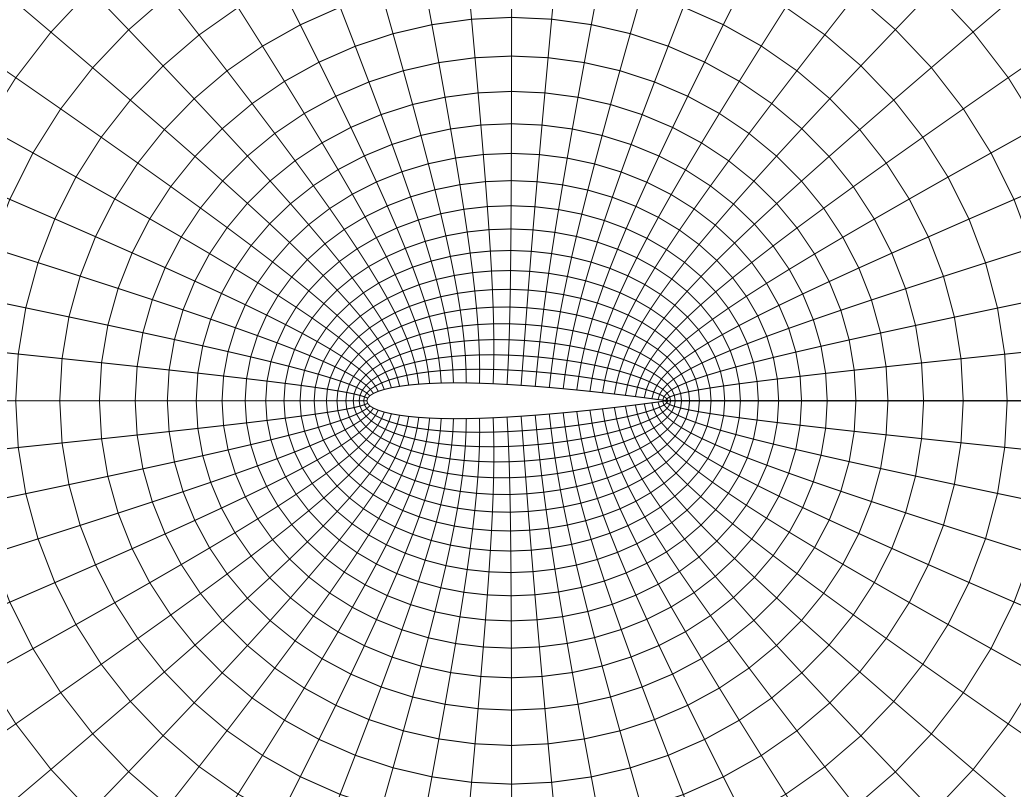


Figure 4. Close-up view of the 64x64 O-mesh.

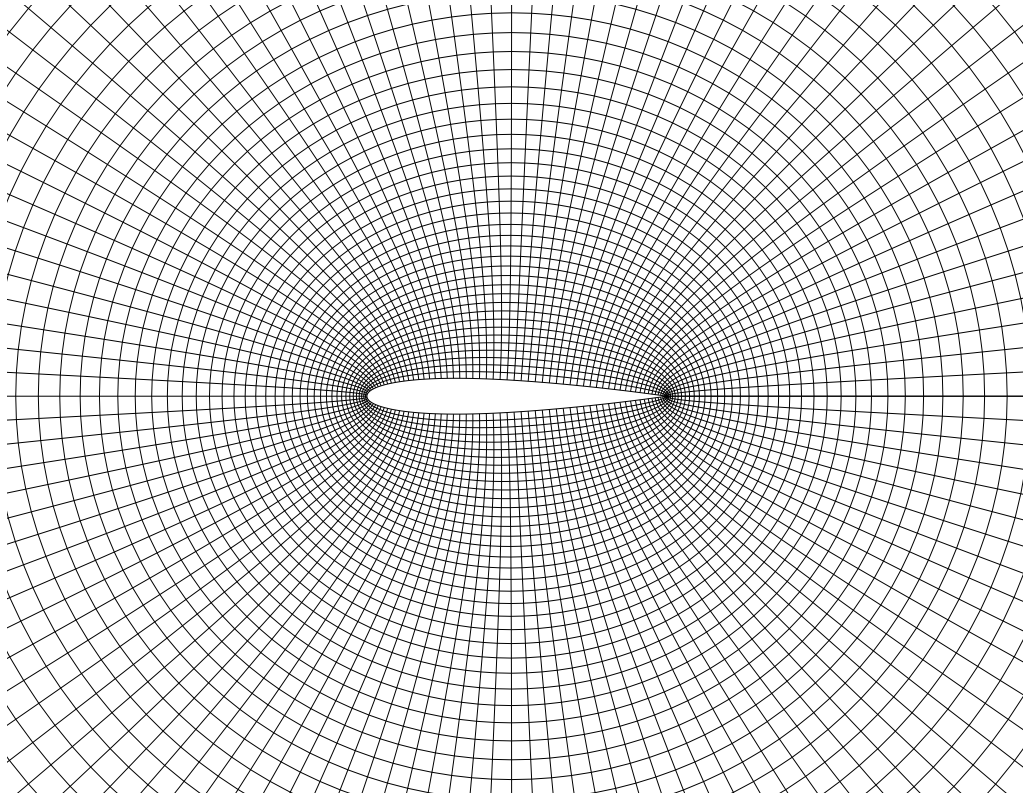


Figure 5. Close-up view of the 128x128 O-mesh.

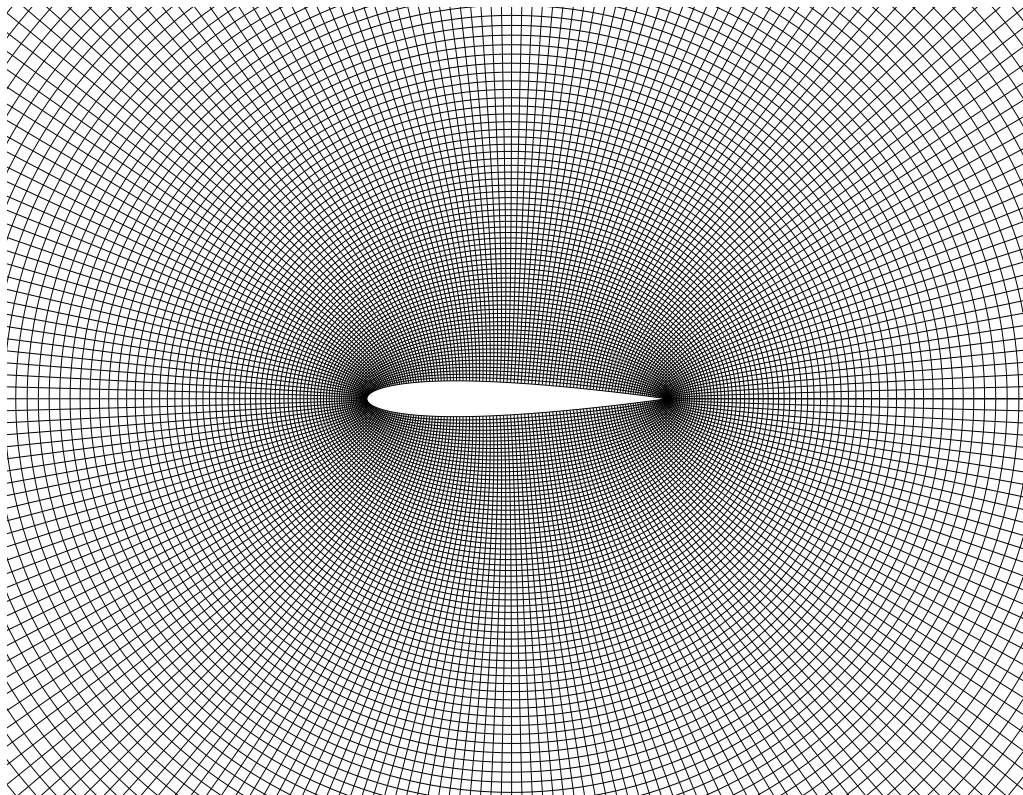


Figure 6. Close-up view of the 256x256 O-mesh.

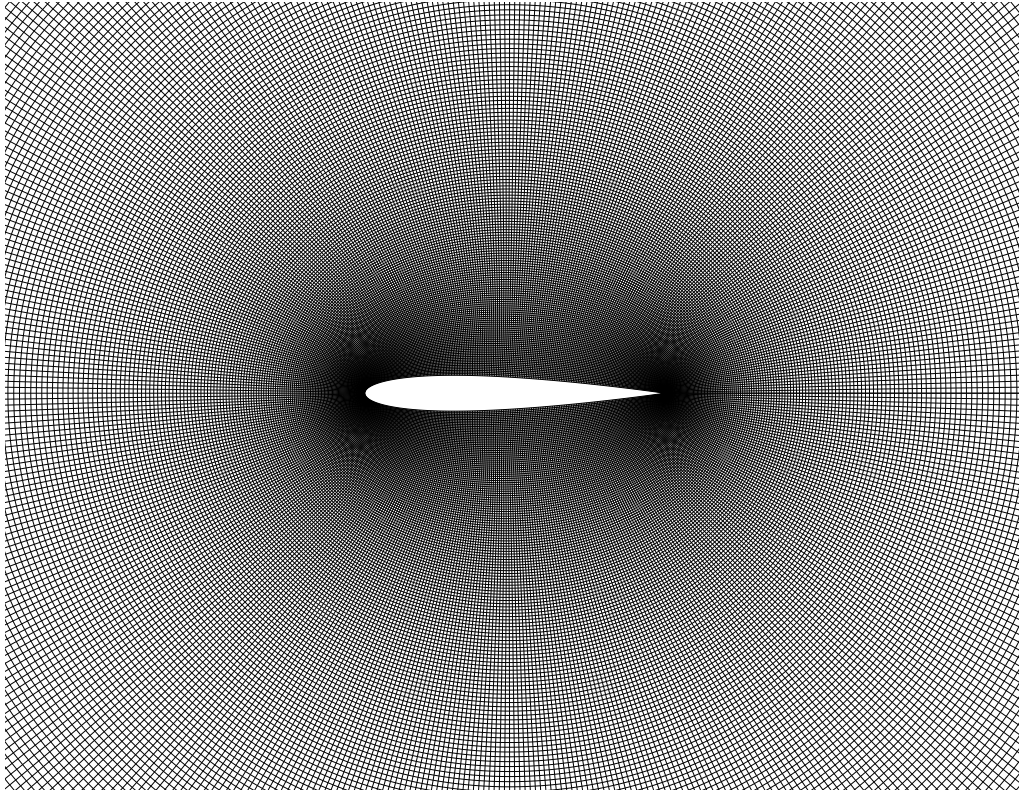


Figure 7. Close-up view of the 512x512 O-mesh.

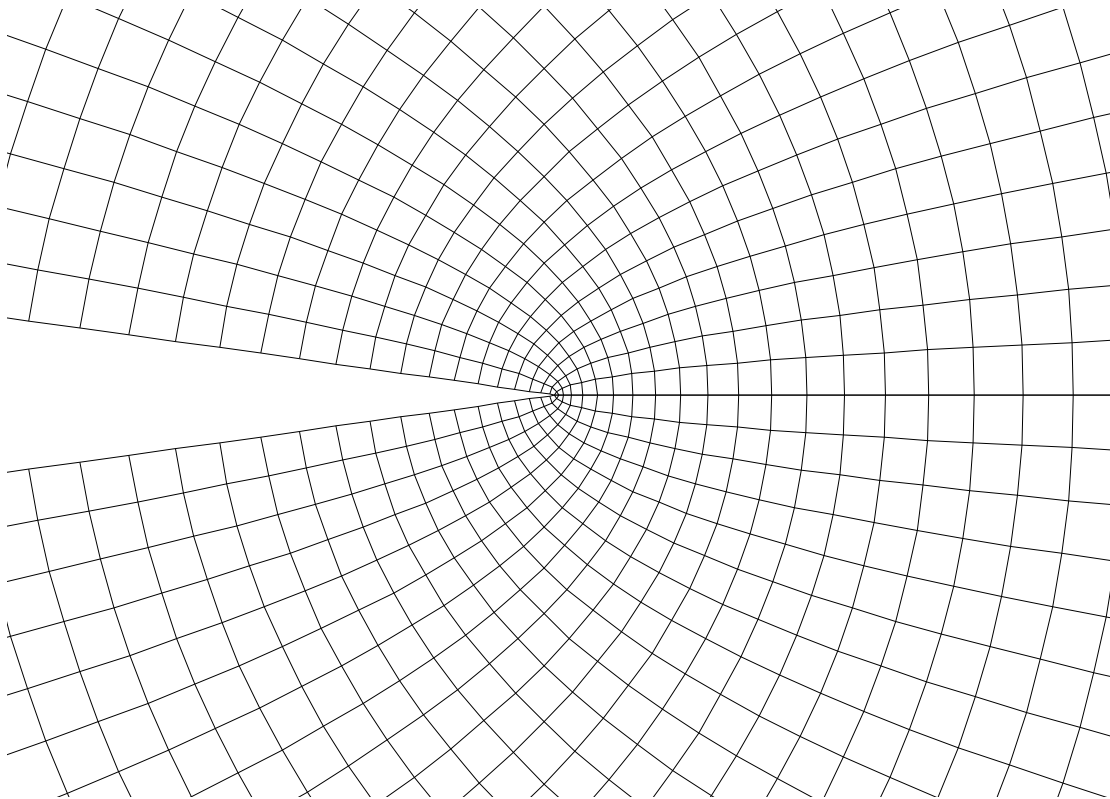


Figure 8. Extreme Close-up view of the 512x512 O-mesh near Trailing Edge.

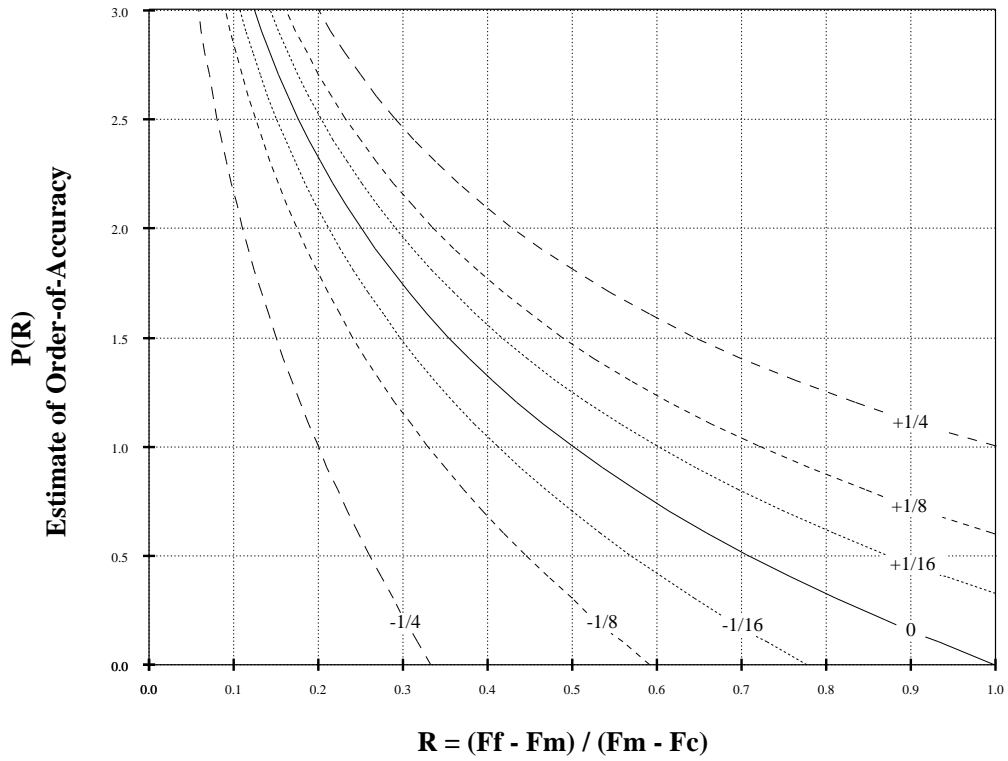


Figure 9. Effect of Discrete-Function-Error on Estimate of Order-of-Accuracy.

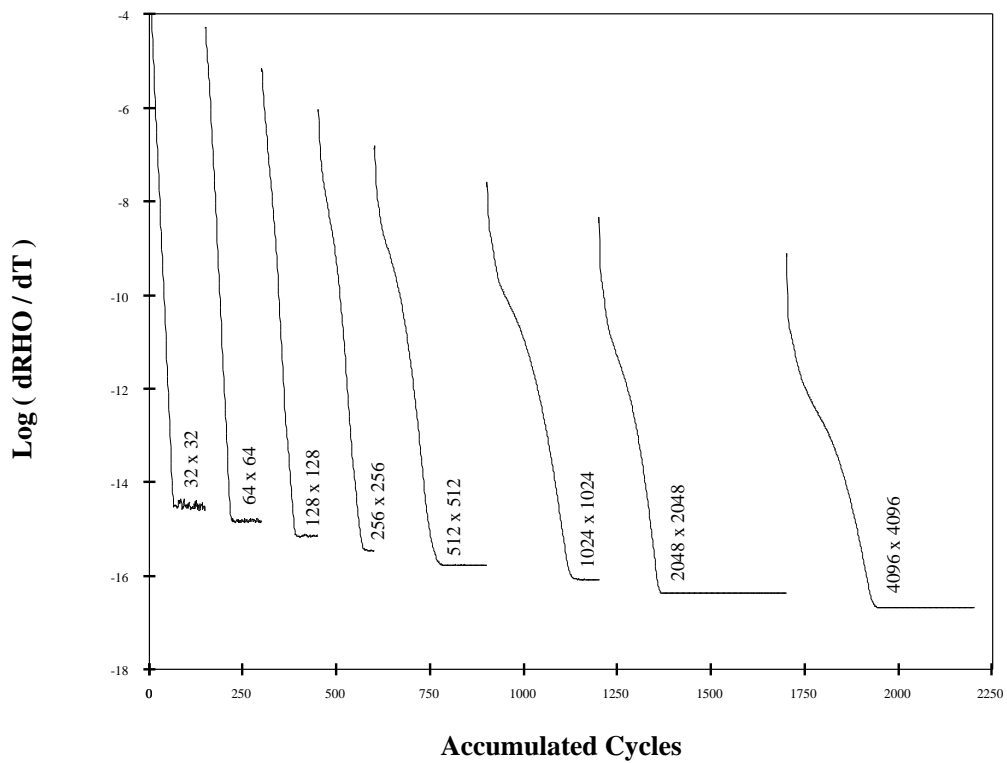


Figure 10. FLO82 Convergence History on All Meshes for $M = 0.50$, and $\alpha = 1.25^\circ$.

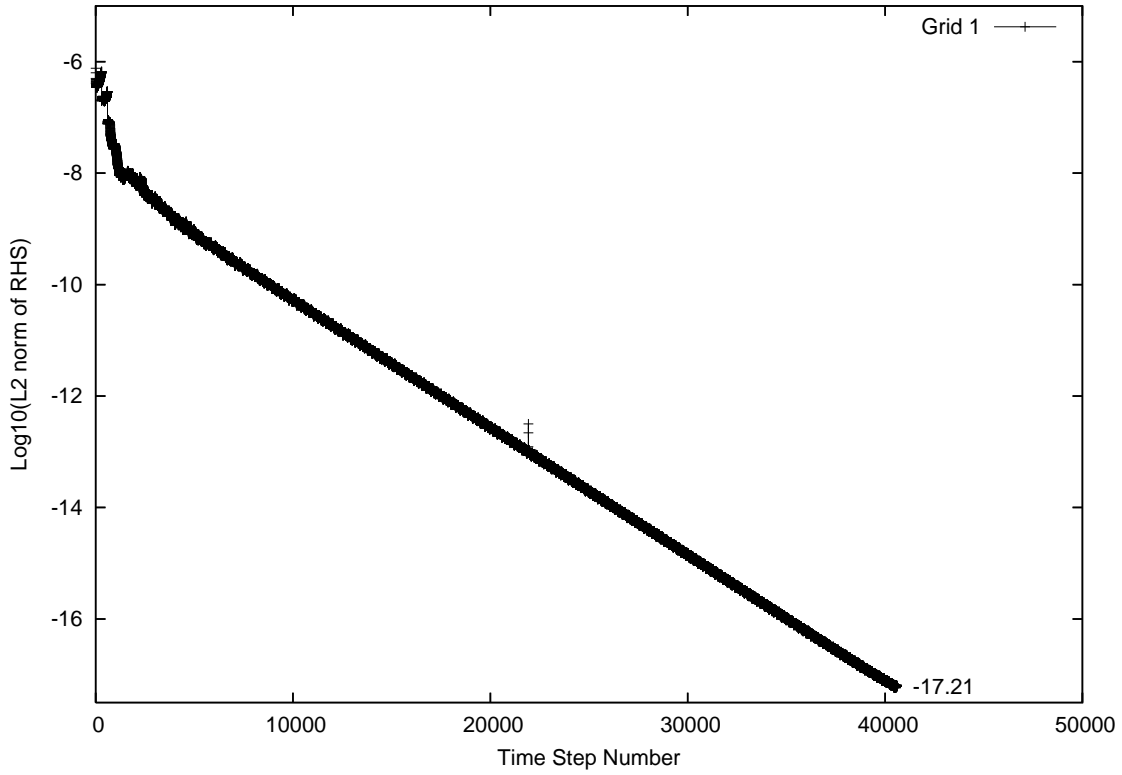


Figure 11. OVERFLOW Convergence History on the Finest Mesh for $M = 0.50$, and $\alpha = 1.25^\circ$.

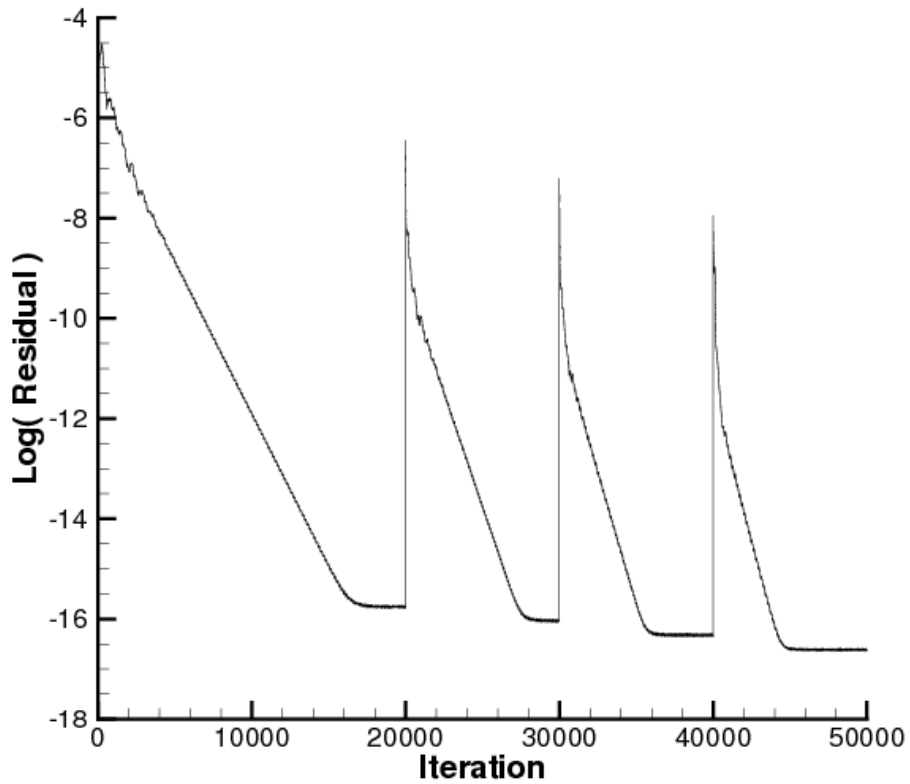
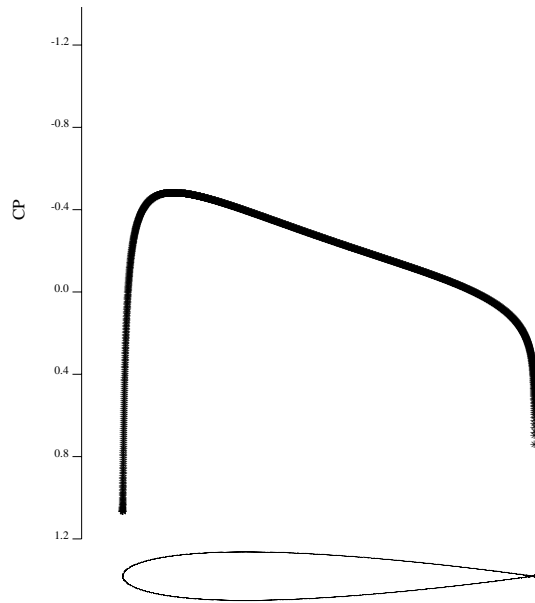


Figure 12. CFL3D Convergence History on Four Meshes for $M = 0.50$, and $\alpha = 1.25^\circ$.



NACA0012 - JCV AR=1 GRID
 MACH 0.500 ALPHA 0.0000000
 CL 0.000000000 CD-0.000000365 CM 0.000000000
 GRID 4096x 4096 NCYC 750 RES 0.116E-12

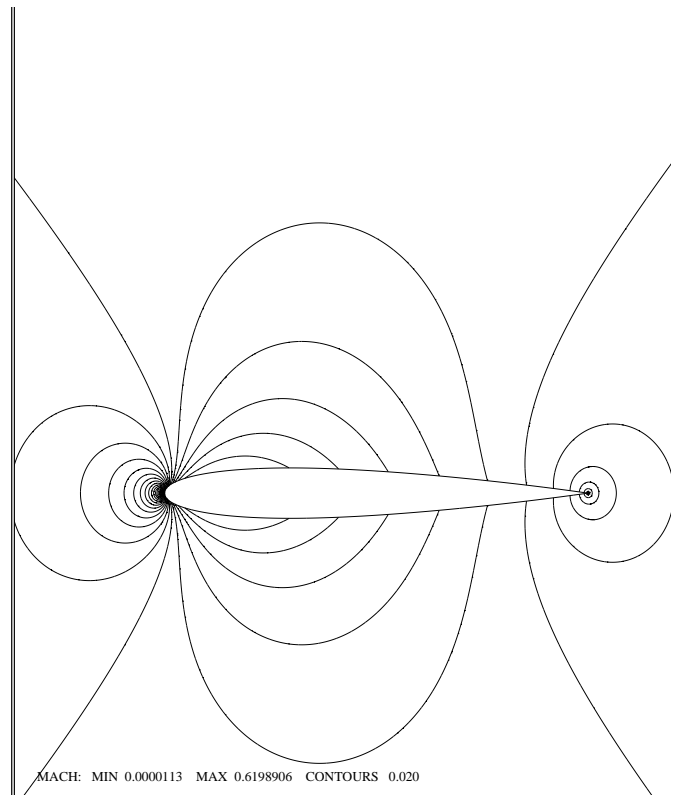
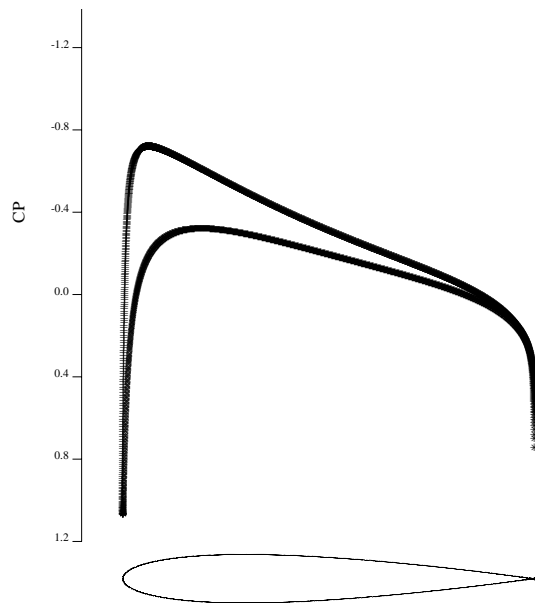


Figure 13. FLO82 Solution on 4096x4096 Mesh at $M = 0.50$, and $\alpha = 0.0^\circ$.



NACA0012 - JCV AR=1 GRID
 MACH 0.500 ALPHA 1.2500000
 CL 0.180347832 CD-0.000000388 CM-0.002269217
 GRID 4096x 4096 NCYC 750 RES 0.258E-12

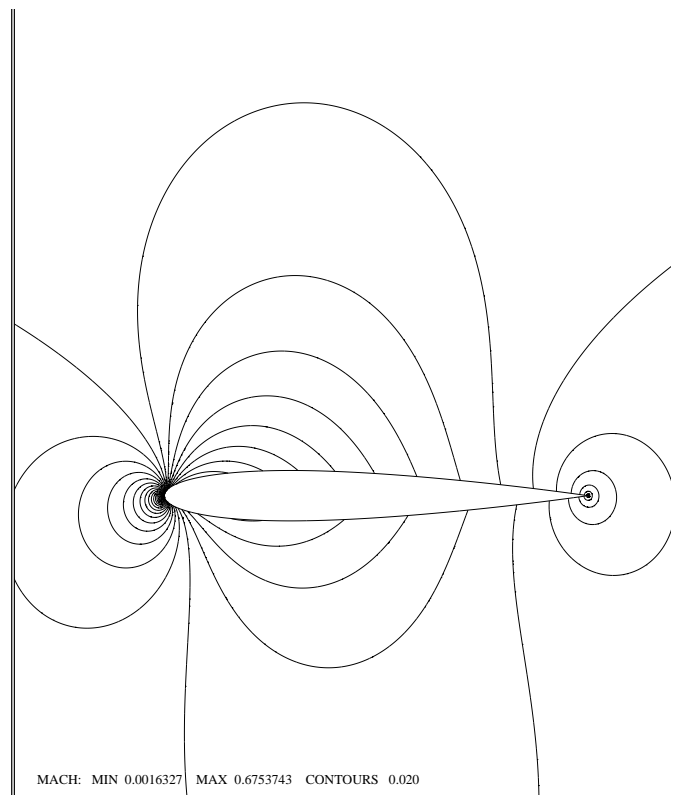
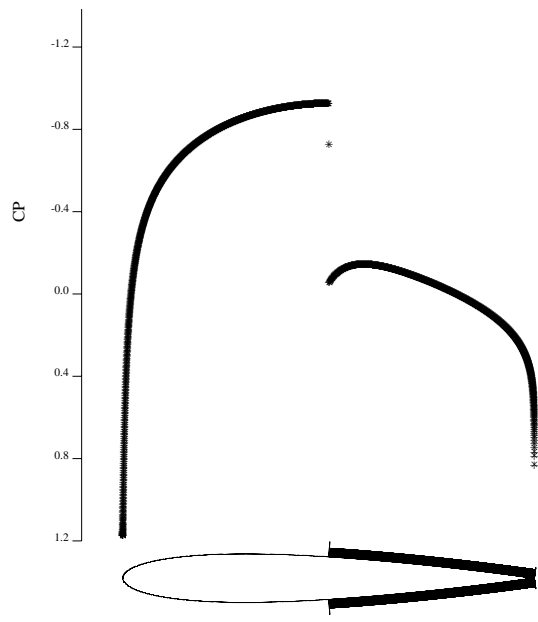


Figure 14. FLO82 Solution on 4096x4096 Mesh at $M = 0.50$, and $\alpha = 1.25^\circ$.



NACA0012 - JCV AR=1 GRID
MACH 0.800 ALPHA 0.0000000
CL 0.000000000 CD 0.008342211 CM 0.000000000
GRID 4096x 4096 NCYC 1000 RED -10.25

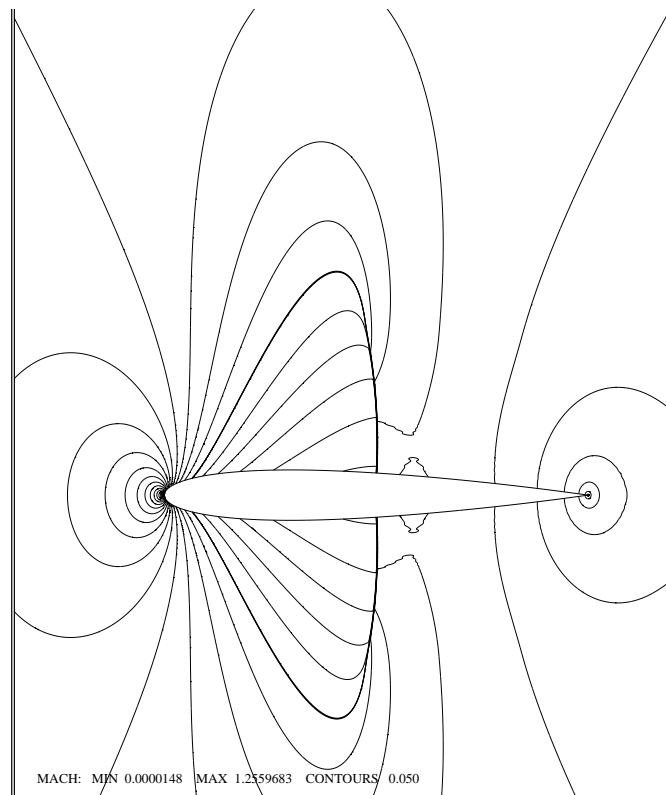
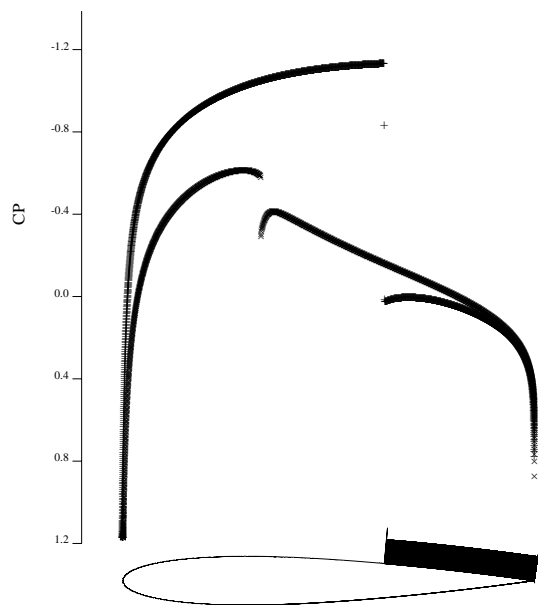


Figure 15. FLO82 Solution on 4096x4096 Mesh at $M = 0.80$, and $\alpha = 0.0^\circ$.



NACA0012 - JCV AR=1 GRID
MACH 0.800 ALPHA 1.2500000
CL 0.357142338 CD 0.022737860 CM -0.039051466
GRID 4096x 4096 NCYC 1000 RED -8.16

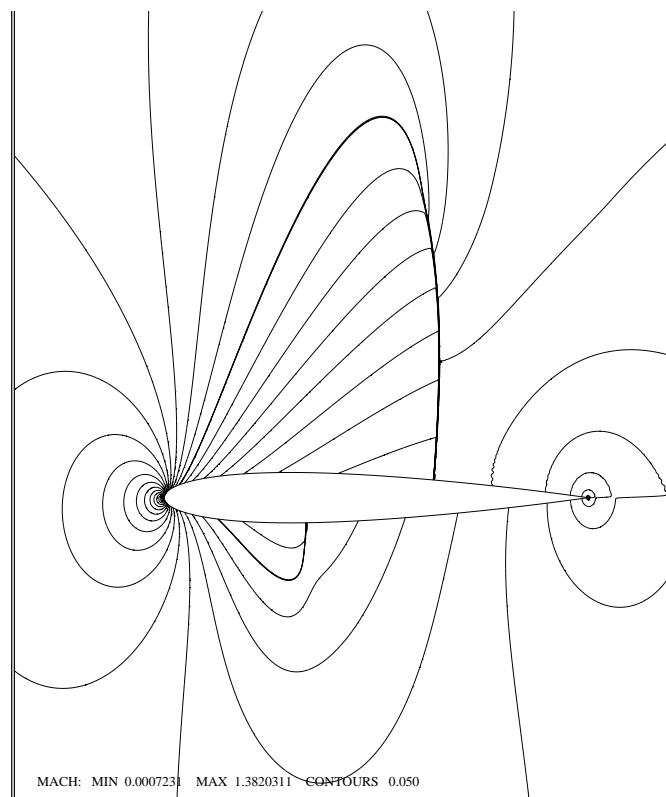


Figure 16. FLO82 Solution on 4096x4096 Mesh at $M = 0.80$, and $\alpha = 1.25^\circ$.

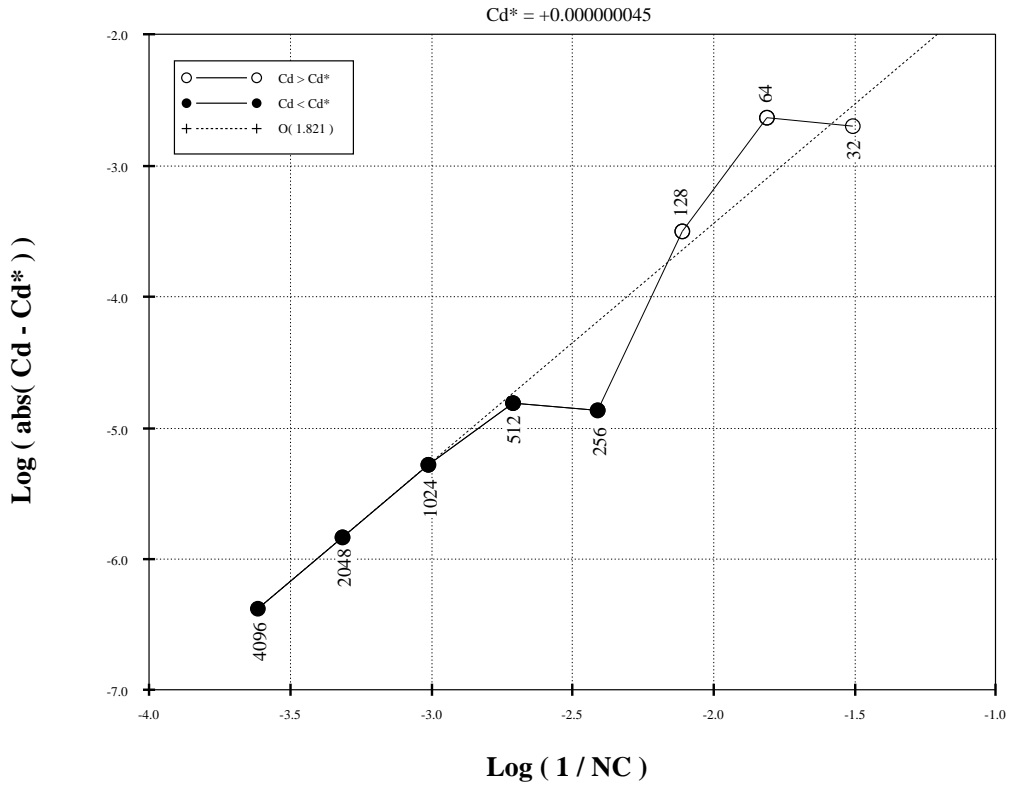


Figure 17. FLO82 Drag Grid-Convergence at $M = 0.50$, and $\alpha = 0.0^\circ$.

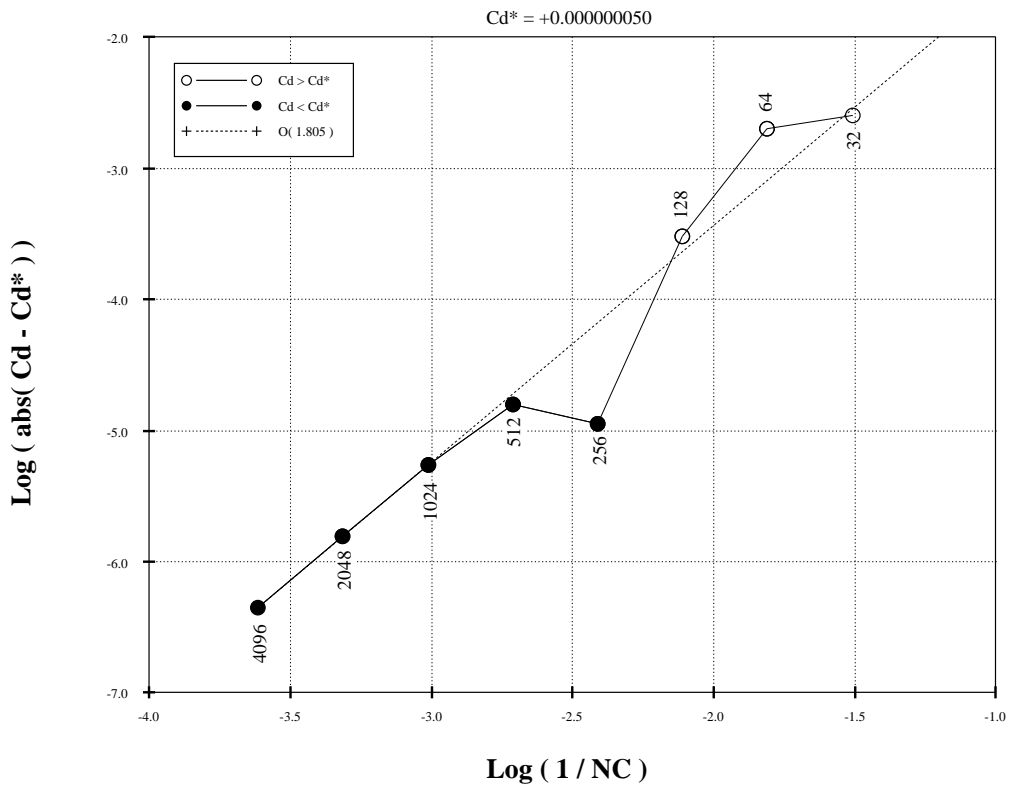


Figure 18. FLO82 Drag Grid-Convergence at $M = 0.50$, and $\alpha = 1.25^\circ$.

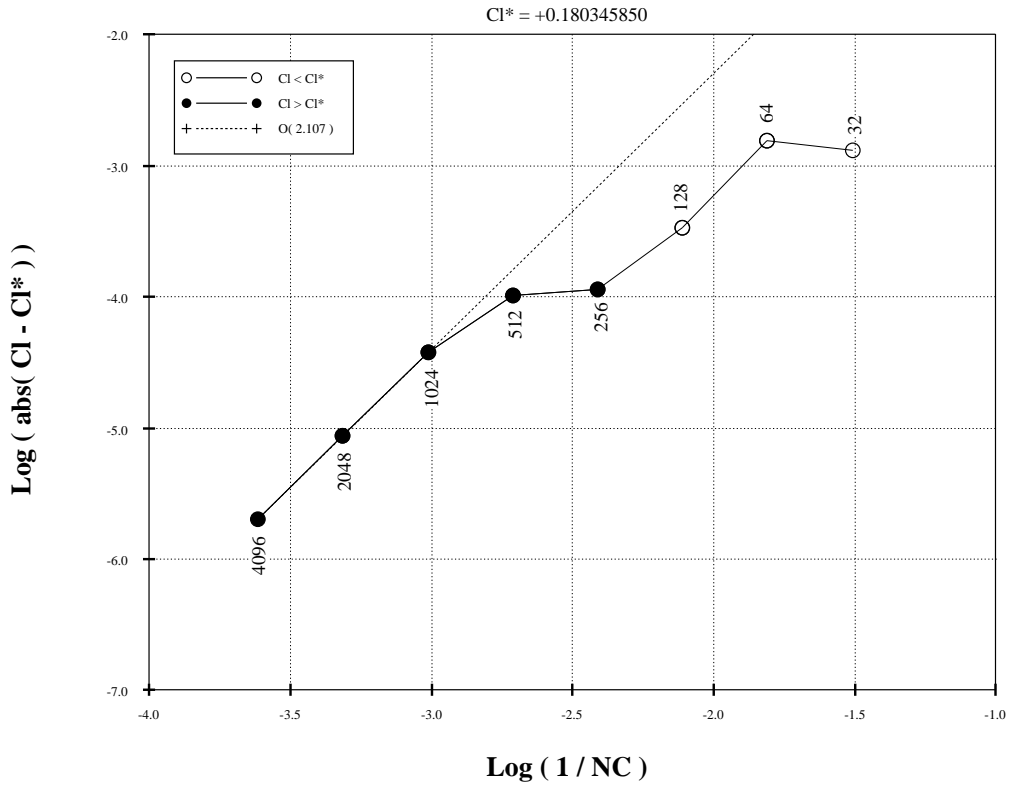


Figure 19. FLO82 Lift Grid-Convergence at $M = 0.50$, and $\alpha = 1.25^\circ$.

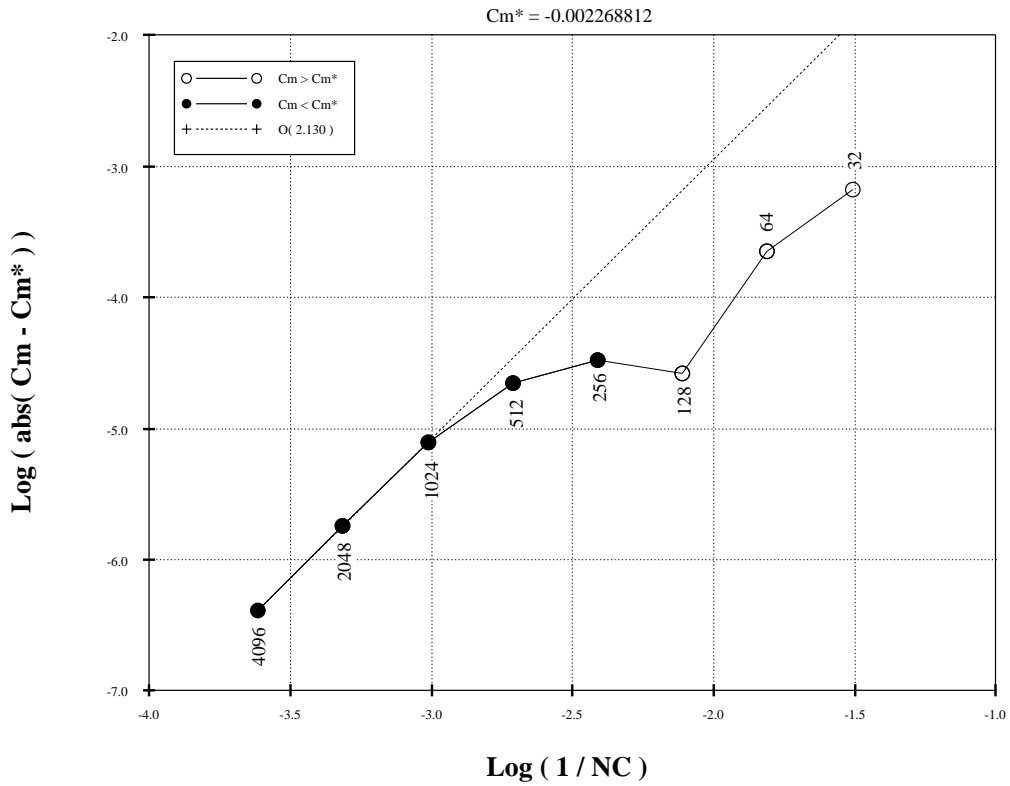


Figure 20. FLO82 Pitching-Moment Grid-Convergence at $M = 0.50$, and $\alpha = 1.25^\circ$.

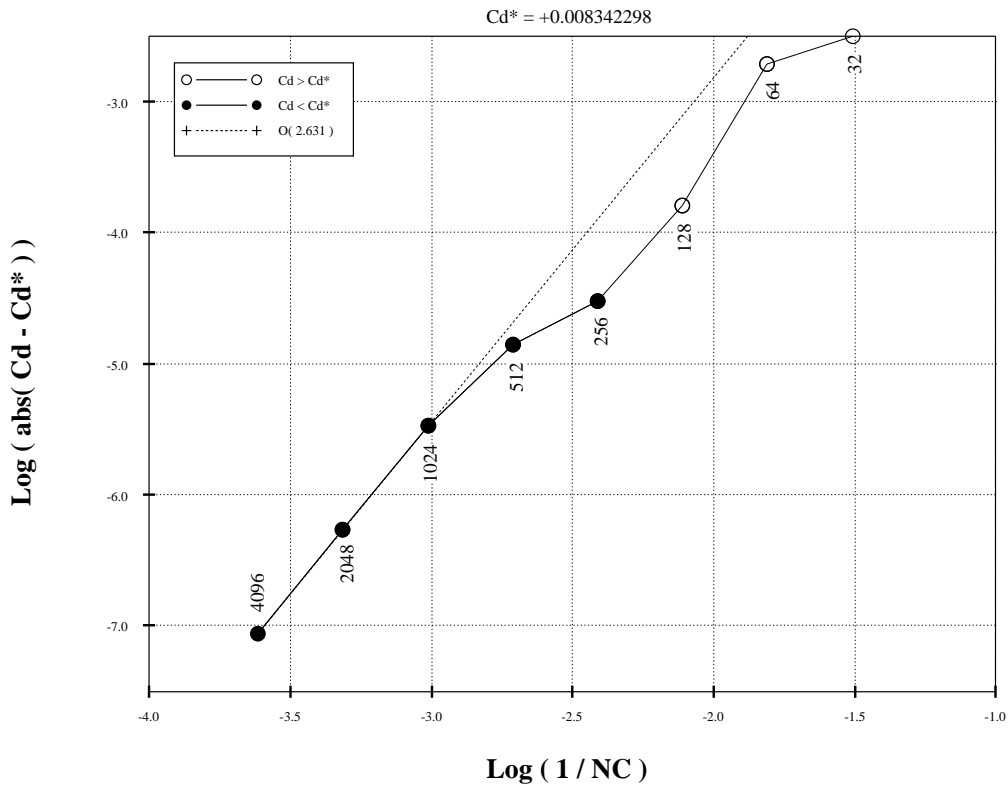


Figure 21. FLO82 Drag Grid-Convergence at $M = 0.80$, and $\alpha = 0.0^\circ$.

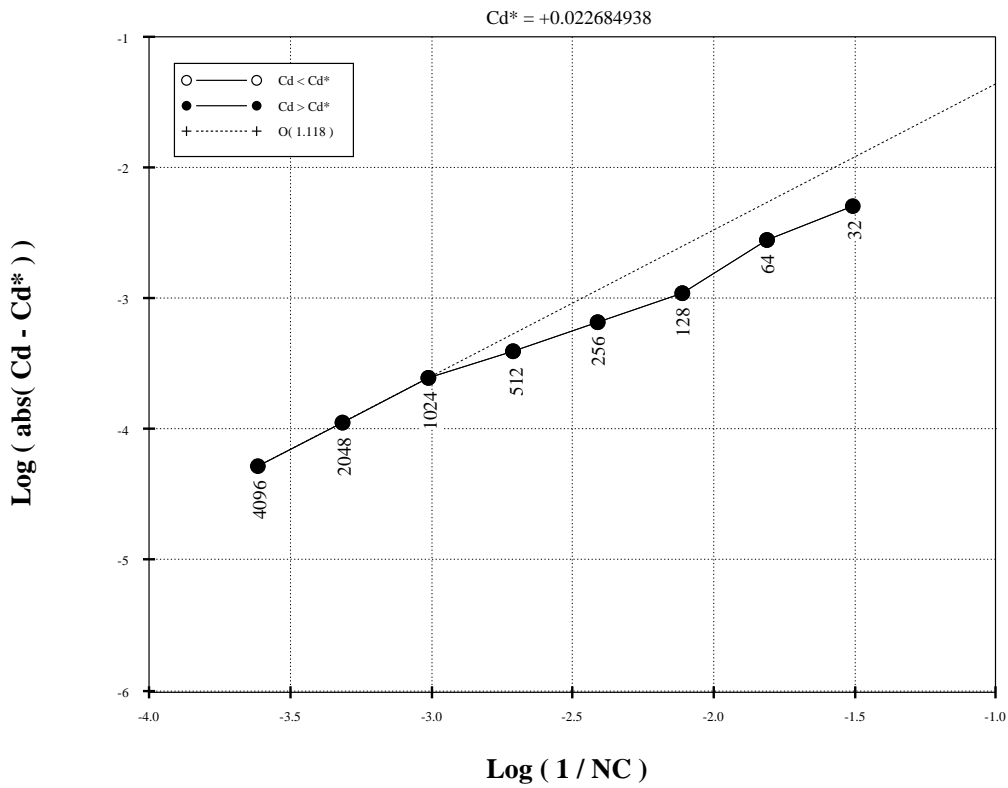


Figure 22. FLO82 Drag Grid-Convergence at $M = 0.80$, and $\alpha = 1.25^\circ$.

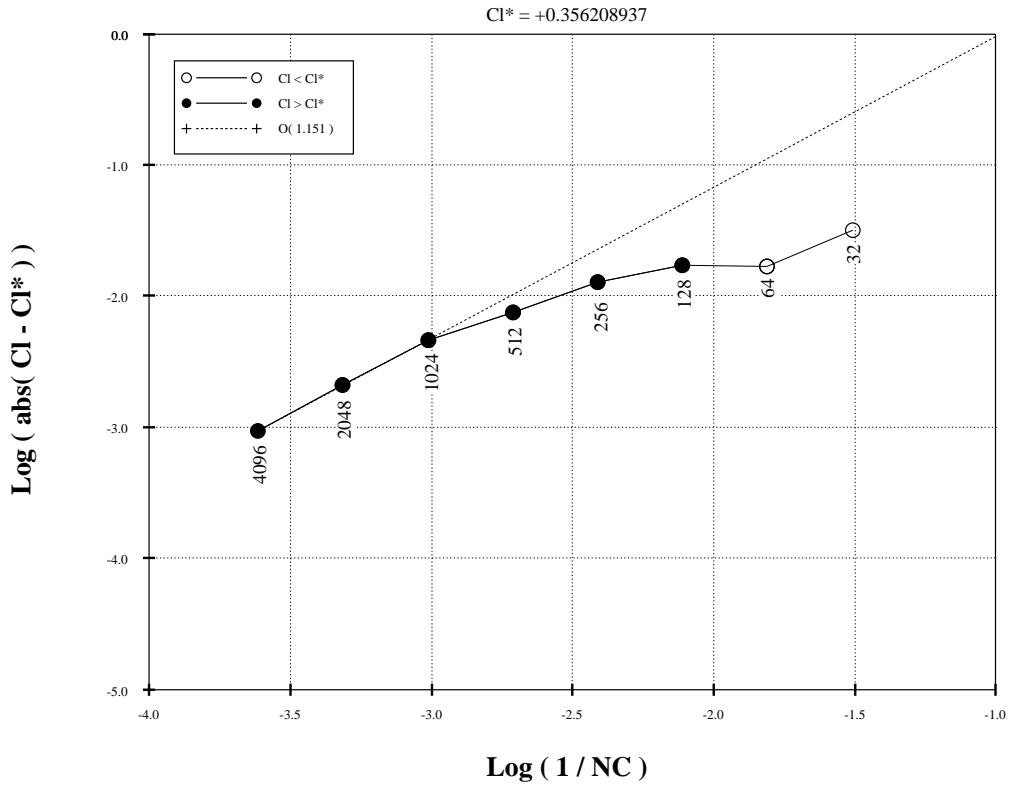


Figure 23. FLO82 Lift Grid-Convergence at $M = 0.80$, and $\alpha = 1.25^\circ$.

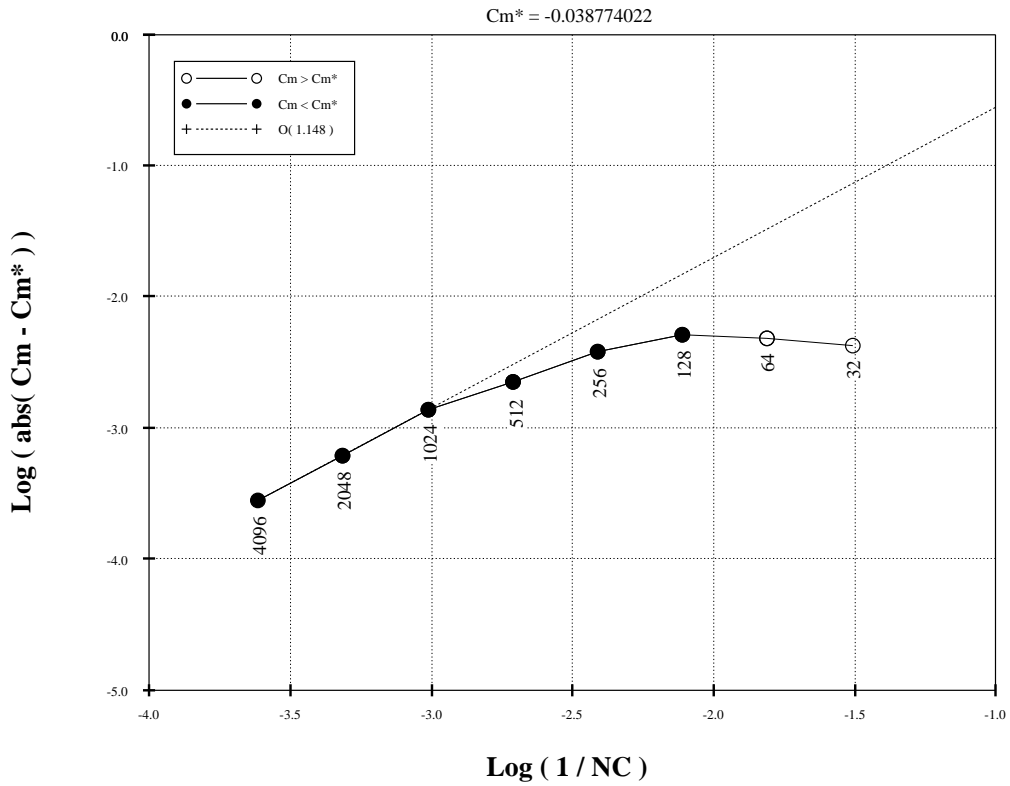


Figure 24. FLO82 Pitching-Moment Grid-Convergence at $M = 0.80$, and $\alpha = 1.25^\circ$.

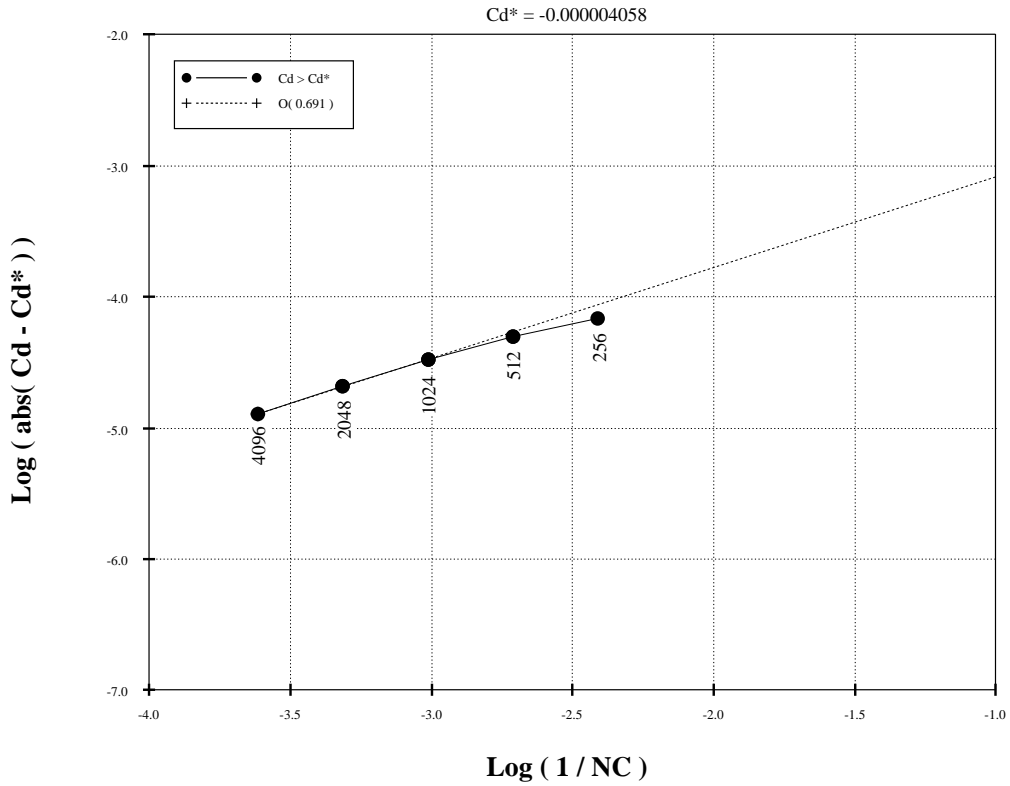


Figure 25. OVERFLOW Drag Grid-Convergence at $M = 0.50$, and $\alpha = 0.0^\circ$.

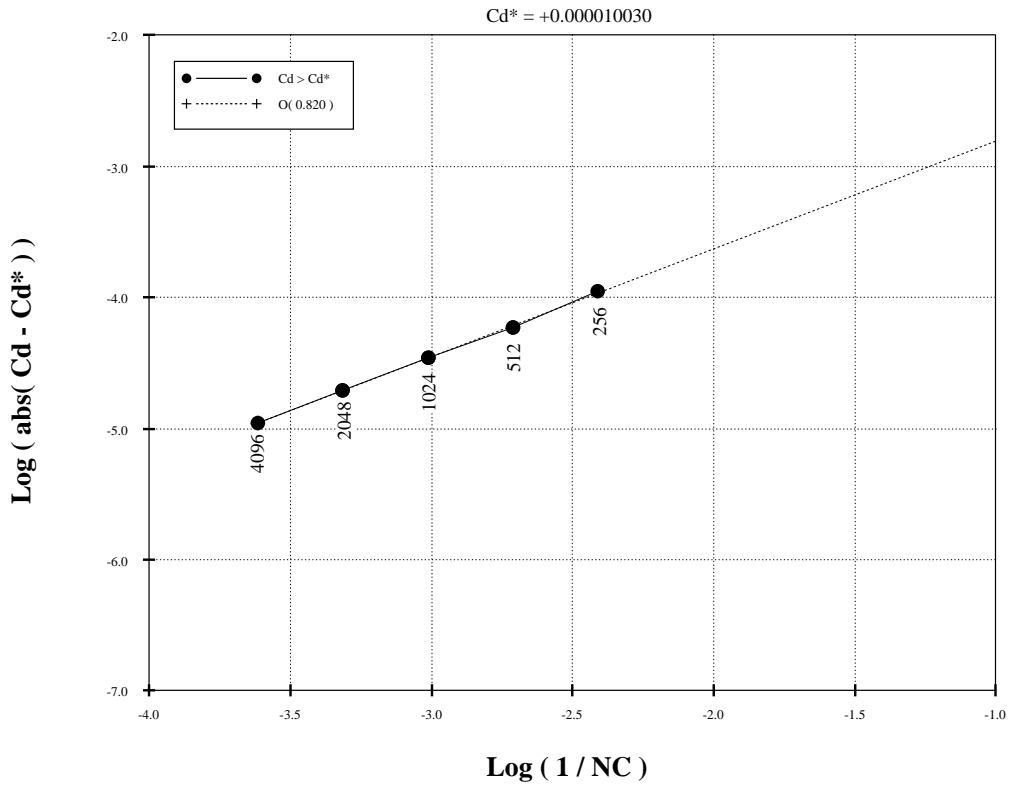


Figure 26. OVERFLOW Drag Grid-Convergence at $M = 0.50$, and $\alpha = 1.25^\circ$.

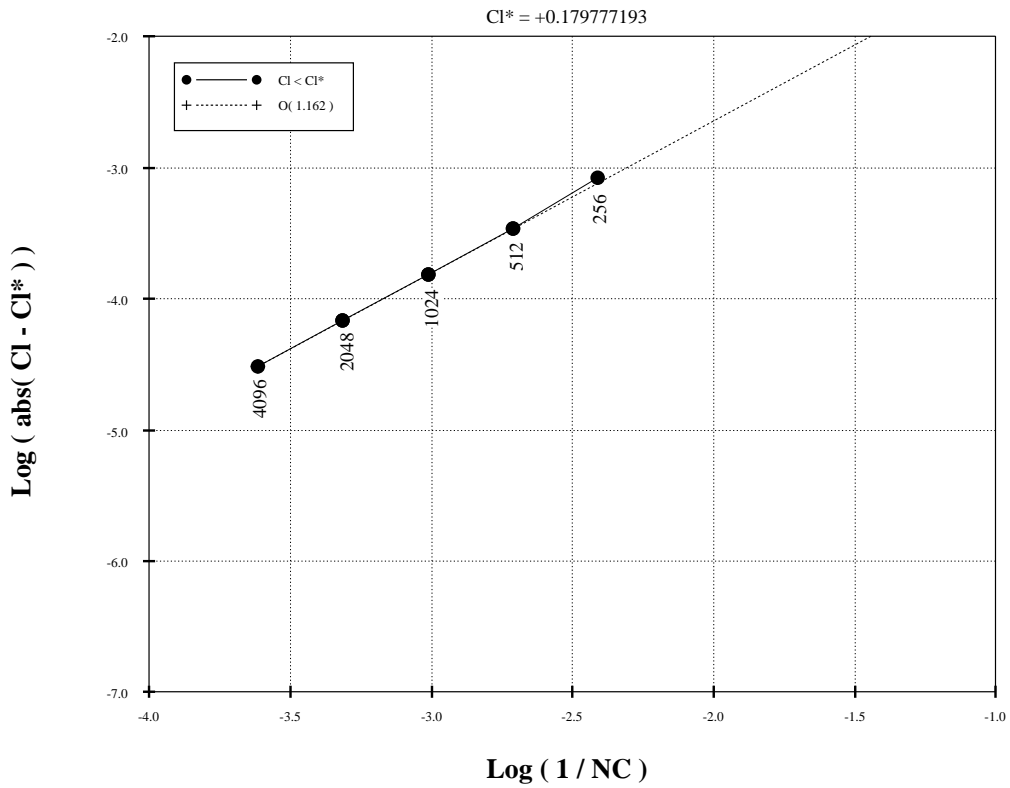


Figure 27. OVERFLOW Lift Grid-Convergence at $M = 0.50$, and $\alpha = 1.25^\circ$.

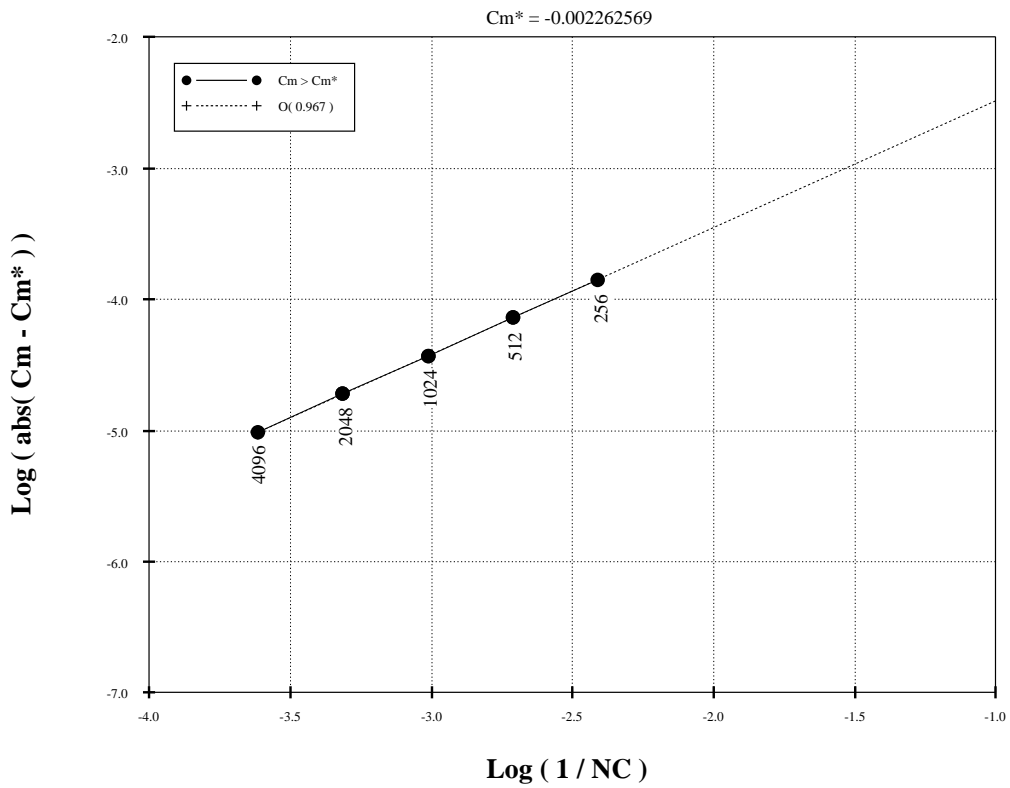


Figure 28. OVERFLOW Pitching-Moment Grid-Convergence at $M = 0.50$, and $\alpha = 1.25^\circ$.

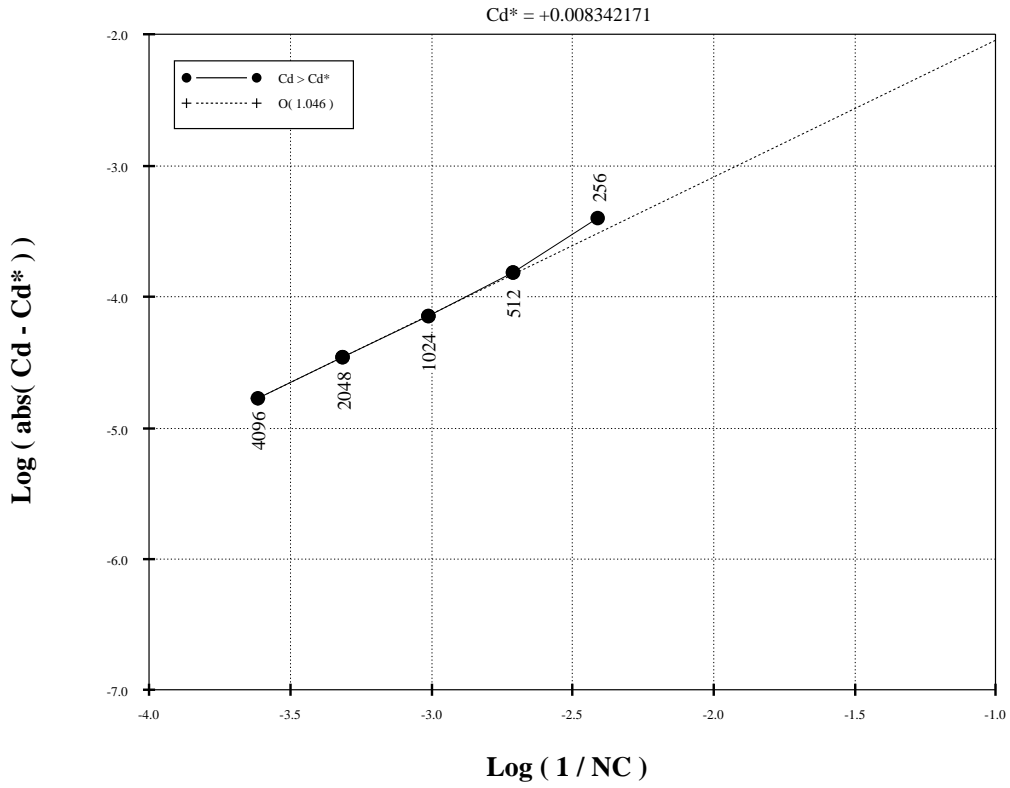


Figure 29. OVERFLOW Drag Grid-Convergence at $M = 0.80$, and $\alpha = 0.0^\circ$.

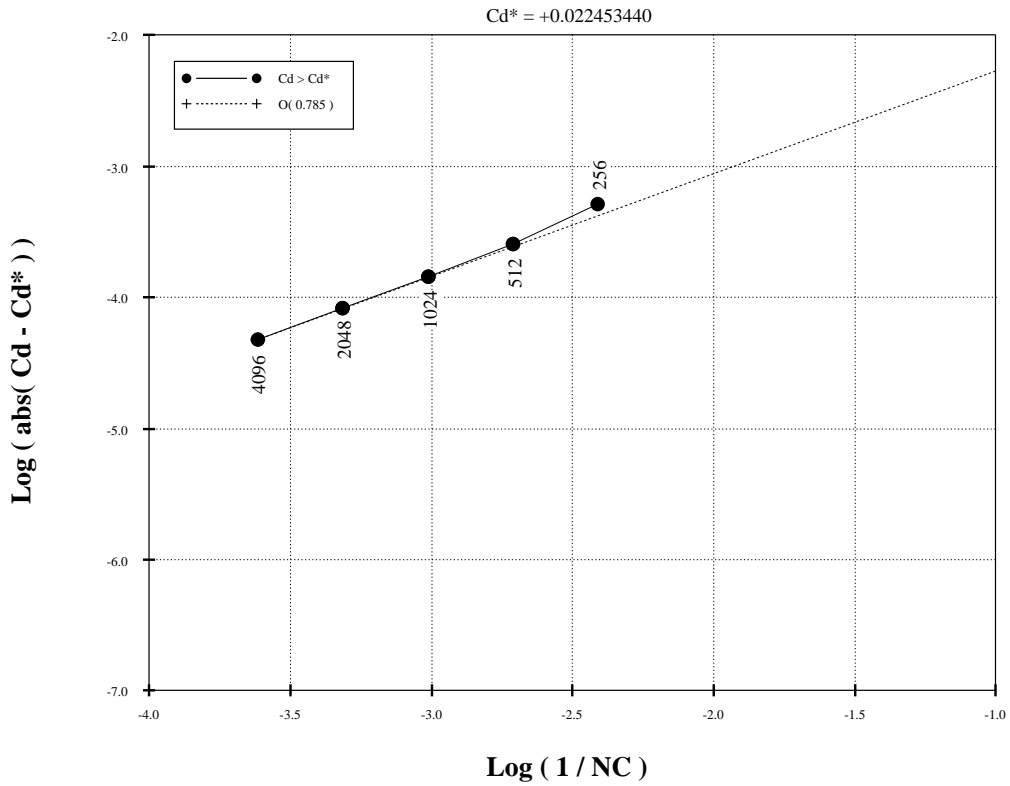


Figure 30. OVERFLOW Drag Grid-Convergence at $M = 0.80$, and $\alpha = 1.25^\circ$.

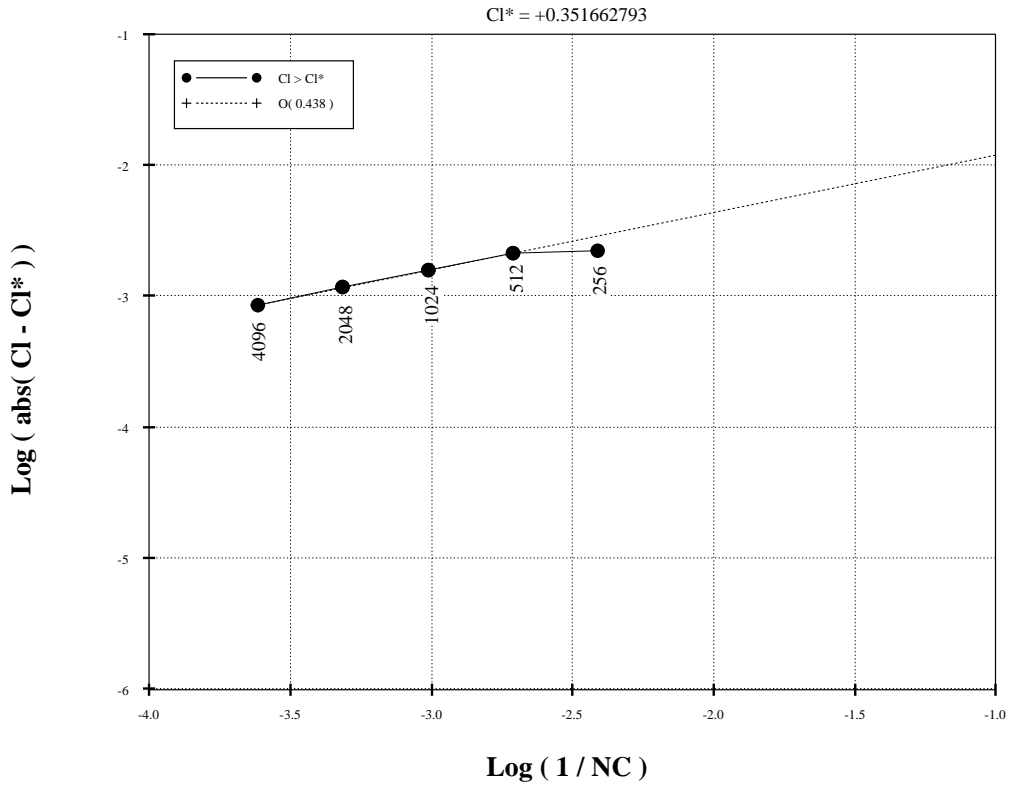


Figure 31. OVERFLOW Lift Grid-Convergence at $M = 0.80$, and $\alpha = 1.25^\circ$.

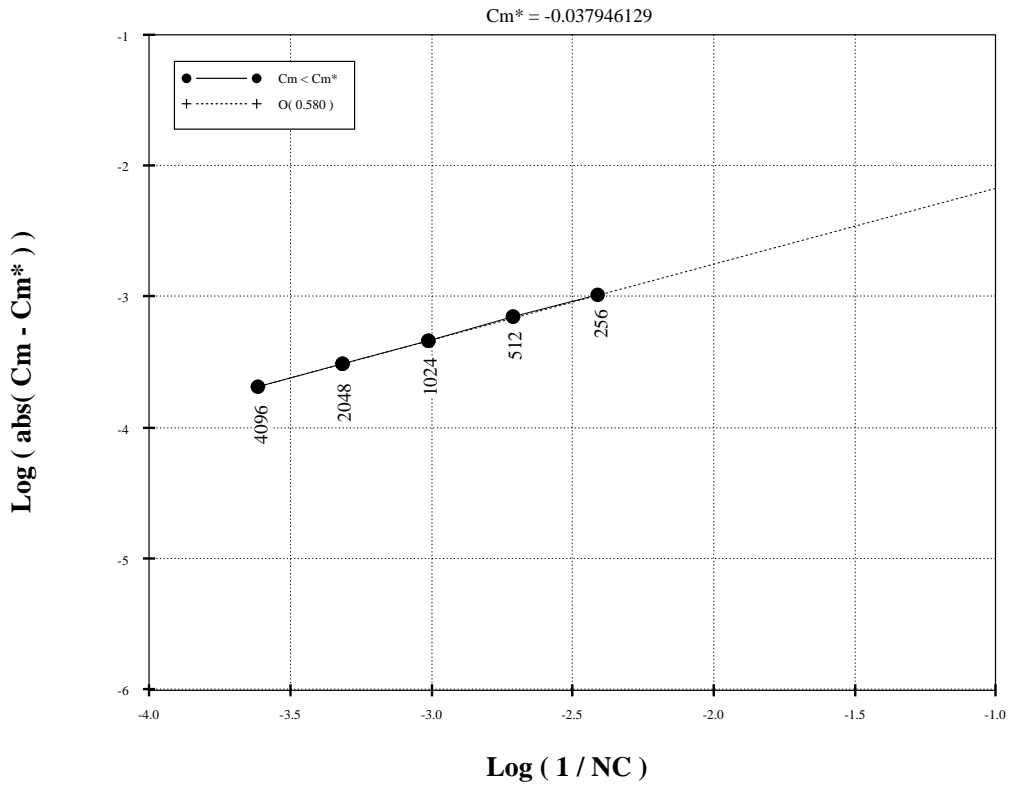


Figure 32. OVERFLOW Pitching-Moment Grid-Convergence at $M = 0.80$, and $\alpha = 1.25^\circ$.

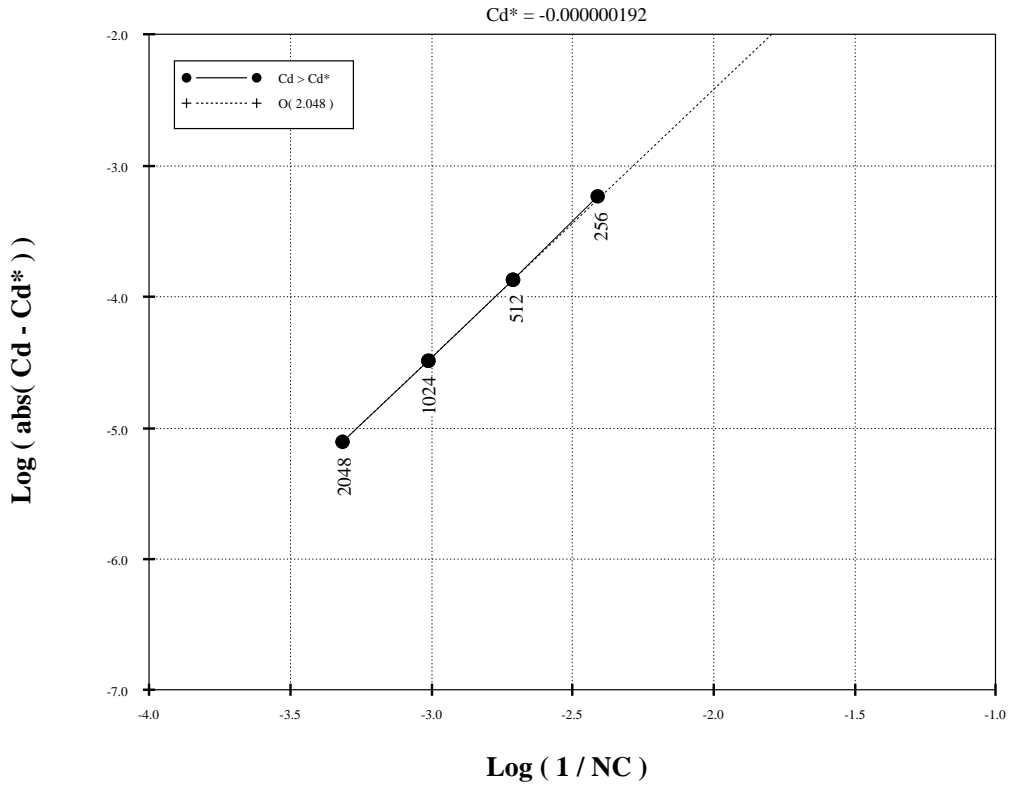


Figure 33. CFL3D Drag Grid-Convergence at $M = 0.50$, and $\alpha = 0.0^\circ$.

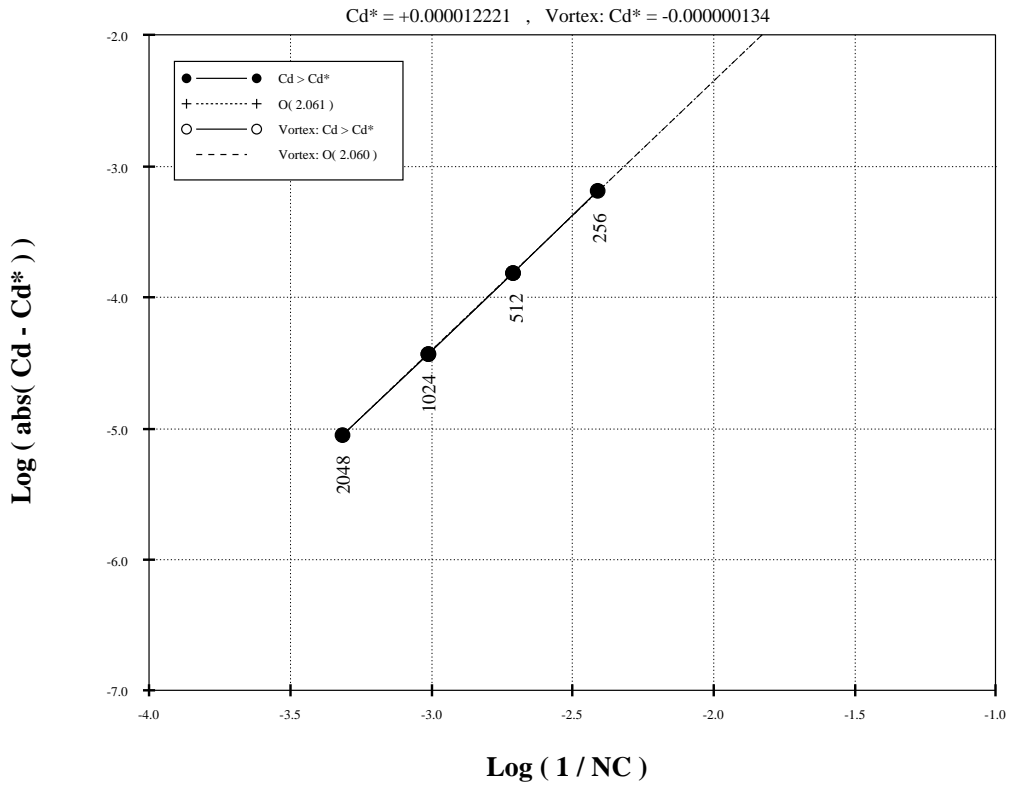


Figure 34. CFL3D Drag Grid-Convergence at $M = 0.50$, and $\alpha = 1.25^\circ$.

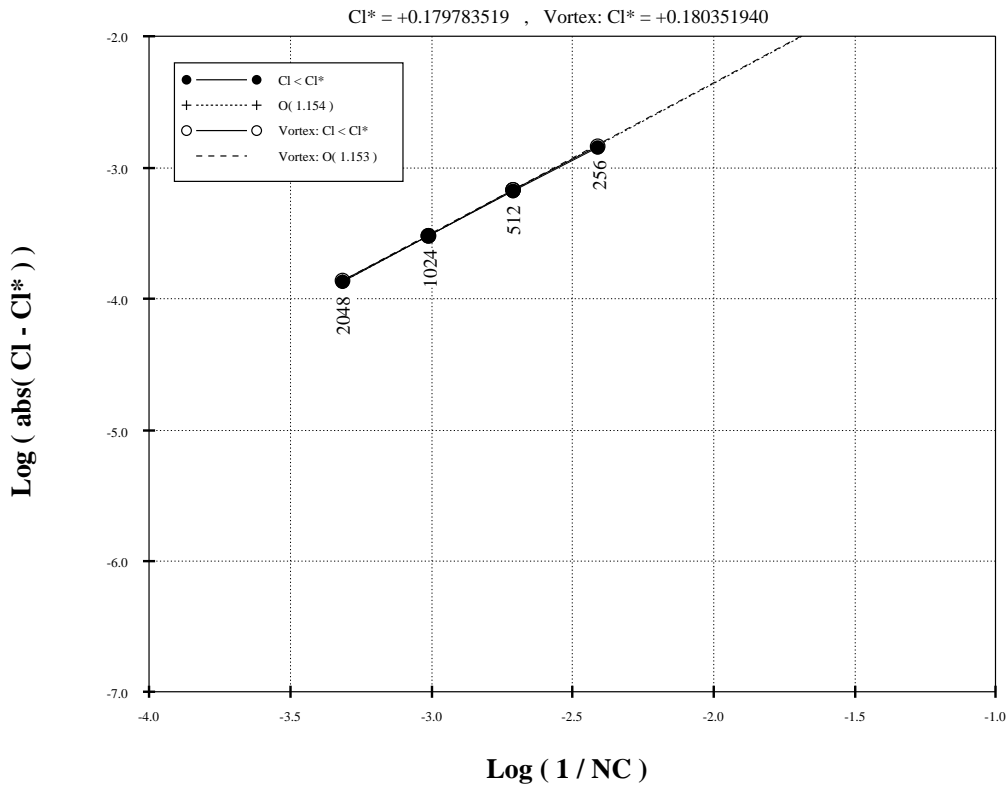


Figure 35. CFL3D Lift Grid-Convergence at $M = 0.50$, and $\alpha = 1.25^\circ$.

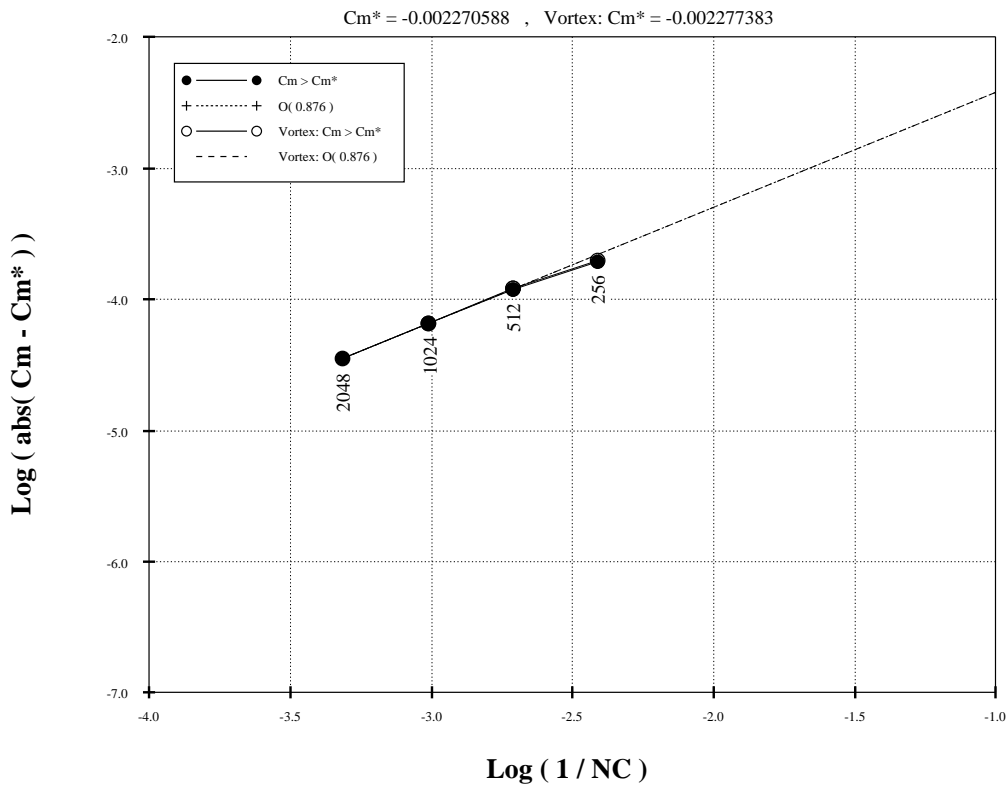


Figure 36. CFL3D Pitching-Moment Grid-Convergence at $M = 0.50$, and $\alpha = 1.25^\circ$.

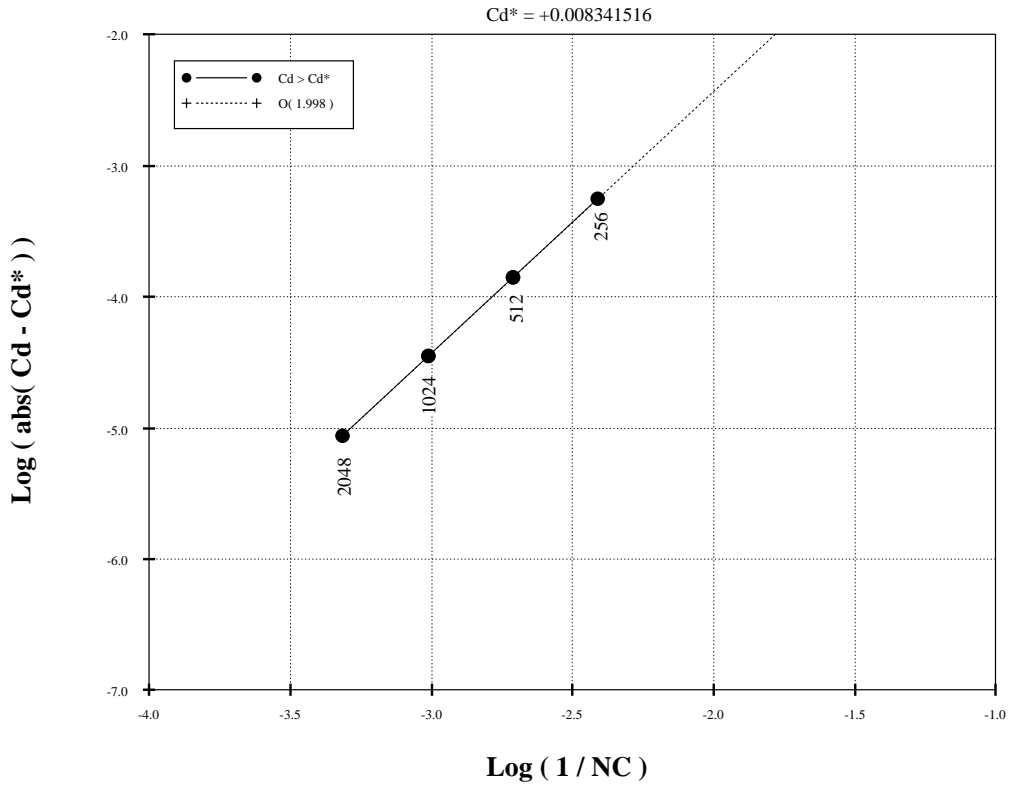


Figure 37. CFL3D Drag Grid-Convergence at $M = 0.80$, and $\alpha = 0.0^\circ$.

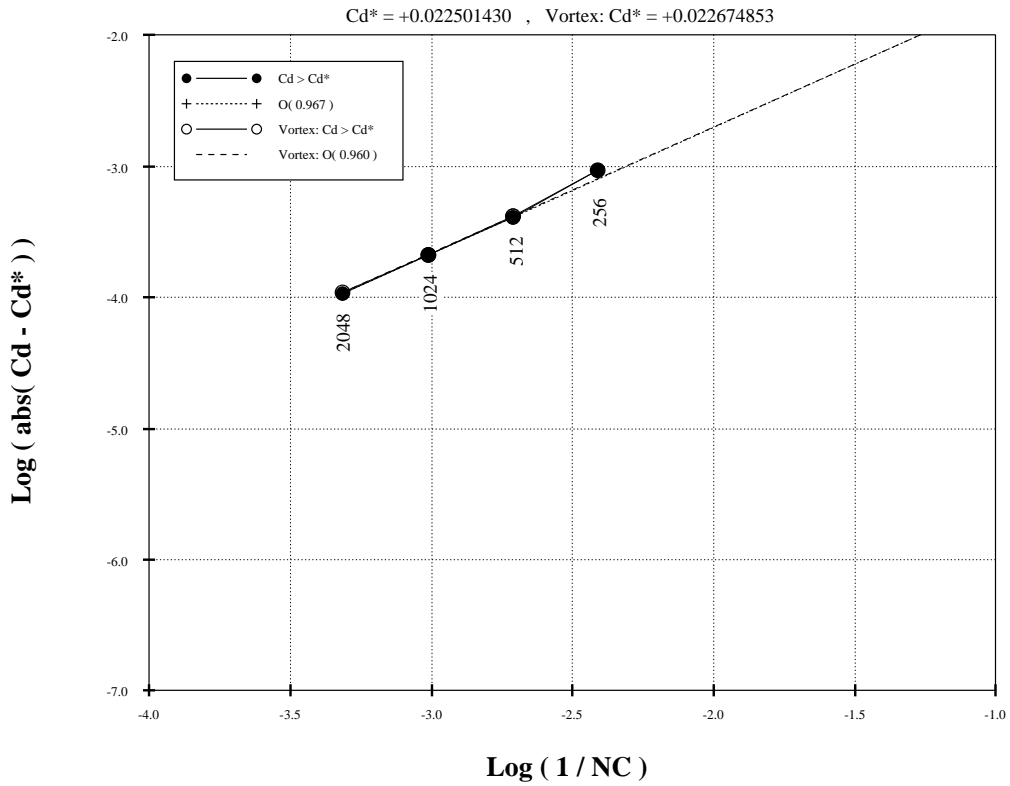


Figure 38. CFL3D Drag Grid-Convergence at $M = 0.80$, and $\alpha = 1.25^\circ$.

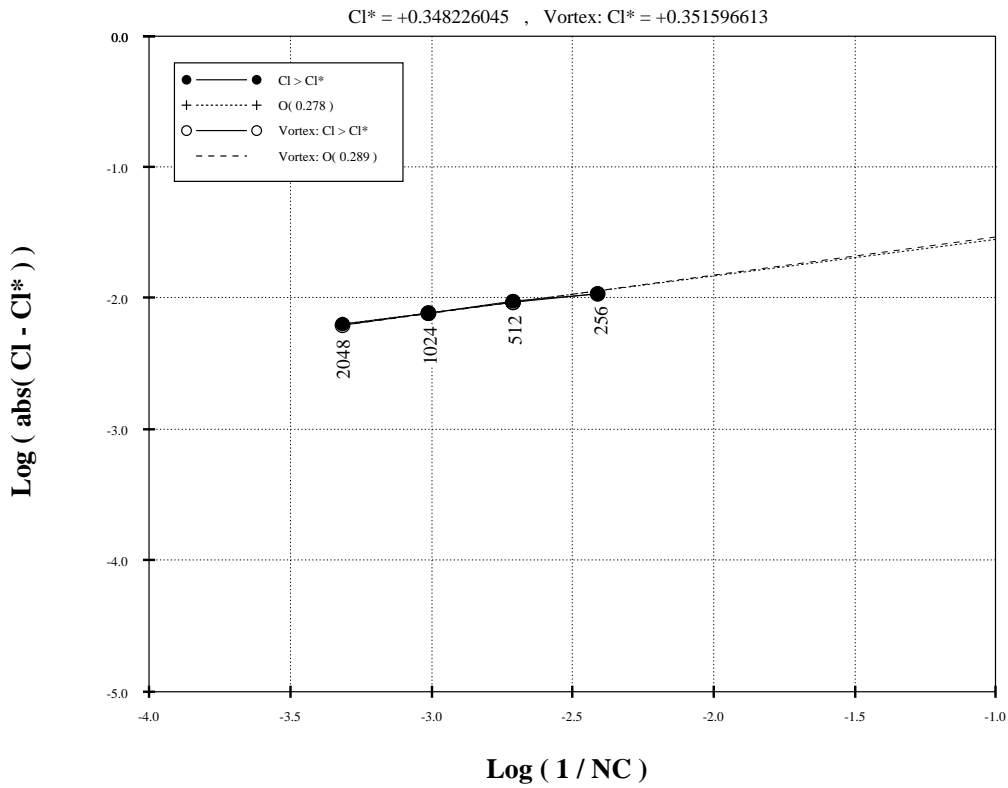


Figure 39. CFL3D Lift Grid-Convergence at $M = 0.80$, and $\alpha = 1.25^\circ$.

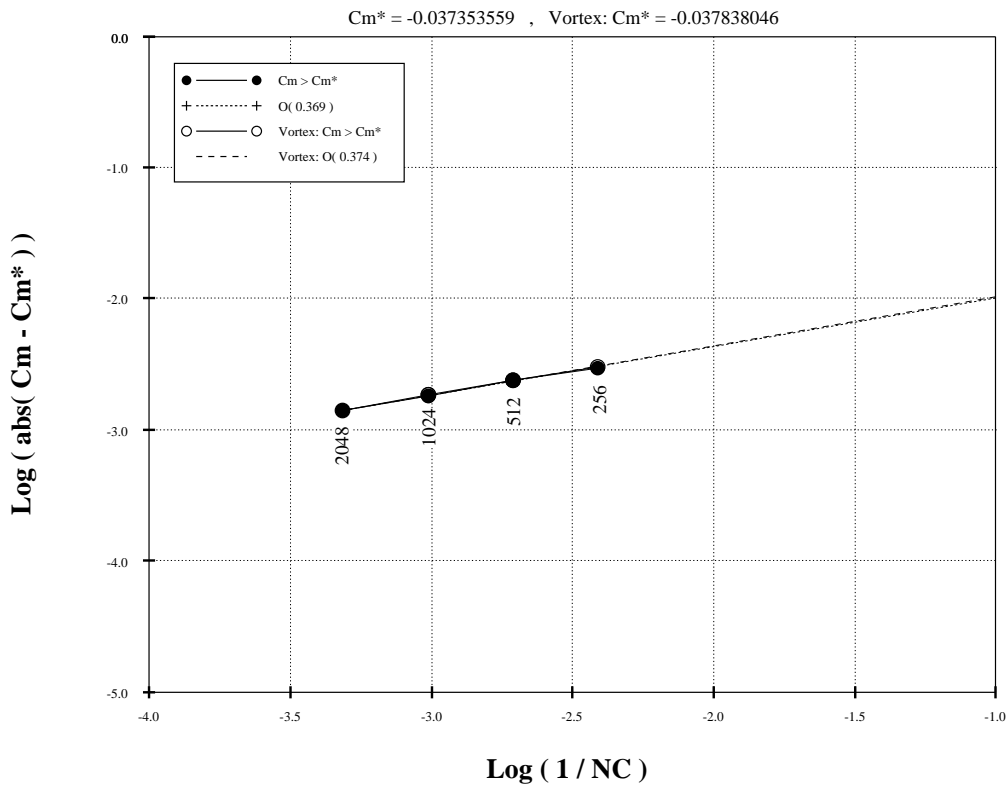


Figure 40. CFL3D Pitching-Moment Grid-Convergence at $M = 0.80$, and $\alpha = 1.25^\circ$.